Soil Carbon Monitoring Using Laser-Induced Breakdown Spectroscopy

Master's Thesis, 18.1.2024

Author:

Joni Ahokas

Supervisors:

Jan Viljanen and Juha Muhonen

JYVÄSKYLÄN YLIOPISTO
UNIVERSITY OF JYVÄSKYLÄ

© 2024 Joni Ahokas
Julkaisu on tekijänoikeussäännösten alainen. Teosta voi lukea ja tulostaa henkilökohtaista käyttöä varten. Käyttö kaupallisiin tarkoituksiin on kielletty. This publication is copyrighted. You may download, display and print it for Your own personal use. Commercial use is prohibited.

Abstract

Ahokas, Joni
Soil Carbon Monitoring Using Laser-Induced Breakdown Spectroscopy
Master's Thesis
Department of Physics, University of Jyväskylä, 2022, 60 pages.

Monitoring soil carbon can be helpful in understanding how different land-use practices sequestrate carbon from the atmosphere. This is important for climate change mitigation as well as the soil well-being. Soil carbon assessment is currently mostly done using dry combustion methods, which require a lot of sample preparation and a laboratory environment. Therefore these methods are not well suited for monitoring purposes, and novel and fast methods for measuring soil carbon concentrations are needed. Laser-induced breakdown spectroscopy is able to remove many of the bottlenecks related to other measurement methods. In this work, optimal measurement parameters are determined and calibration of a laser-induced breakdown spectroscopy setup is performed using a set of samples reference measured with dry combustion. Optimal measurement parameters, including laser wavelength, laser energy, spectrometer delay and exposure time were found and two calibration models for two different sets of samples were created based on these parameters.

Keywords: laser-induced breakdown spectroscopy, LIBS, soil carbon, carbon sequestration, climate change

Contents

Abstract **3**

Abbreviations **6**

1 Introduction **6**

2 Climate change and soil **8**
2.1 Climate change 8
2.2 Carbon cycle 8
2.3 Removal of carbon from the atmosphere by soil management 10

3 Measurement techniques to determine soil carbon concentration **12**
3.1 Infrared spectroscopy 12
3.2 Near-infrared spectroscopy 14
3.3 Eddy covariance method 14
3.4 Elemental determination by combustion 15
3.5 Inductively coupled plasma atomic emission spectrometry 15
3.6 Laser-induced breakdown spectroscopy 16

4 Theoretical background of laser-induced breakdown spectroscopy **20**
4.1 Electromagnetic radiation 20
4.2 Absorption and emission of light 21
4.3 Laser radiation 22
4.4 Laser-induced plasmas 23
4.5 Spectral line shape and fitting 26
4.6 Electron density and plasma temperature 29

5 Soils and sample preparation **32**
5.1 Characterization of soils 32
5.2 Sample preparation 34

6 Experimental arrangement **36**
6.1 Instrumentation 37
6.2 Signal acquisition, delay, and energy control 39
6.3 Elements of interest 40

7 Measurements **41**
7.1 Signal processing 42
7.2 Optimal gate delay 42
7.3 Optimal beam energy 45
7.4 Calibration curves 46
7.5 Wavelength dependency 49
7.6 Effects of soil moisture on the signal 50
7.7 Plasma temperature and electron density 51

8 Conclusions **54**

References **60**

Abbreviations

AES - atomic emission spectroscopy
AFOLU - agriculture, forestry, and other land use
EDTA - ethylenediaminetetraacetic acid
FFT - fast Fourier-transform
FIR - far-infrared
FTIR - Fourier-transform infrared (spectroscopy / spectrometer)
FWHM - full width at half maximum
GEO - geotekninen (maaperän luokittelu)
GHG - greenhouse gas
GPP - gross primary product
GTK - geologian tutkimuskeskus
ICP-AES - inductively coupled plasma atomic emission spectroscopy
ICP-MS - inductively coupled plasma mass spectroscopy
IPCC - intergovernmental panel on climate change
IR - infrared
IUPAC - International Union of Pure and Applied Chemistry
LIBS - laser-induced breakdown spectroscopy
LIP - laser-induced plasma
LOD - limit of detection
LTE - local thermodynamic equilibrium
MIR - mid-infrared
NBP - net biome production
Nd:YAG - neodymium-doped yttrium aluminium garnet
NDIR - nondispersive infrared
NEP - net ecosystem production
NIR - near-infrared
NIST - National Institute of Standards and Technology
NPK - nitroge, phosphorus, potassium
NPP - net primary product
OM - organic matter
ppb - parts per billioin
ppt - parts per trillion
RT - rakennustekninen (maaperän luokittelu)
SOC - soil organic carbon
SIC - soil inorganic carbon
TOC - total organic carbon
USDA - United States Departmet of Agriculture
UV - ultraviolet
VIS - visible
WRB - World Reference Base for Soil Resources

1 Introduction

When measuring a sample, we obtain information in either qualitative or quantitative form. Qualitative can mean things such as *which* elements are present in the sample and quantitative can mean for example *how much* of some element is present in the sample. There are many different methods for determining elemental compositions and concentrations from samples. Samples can vary considerably from one to another: they can be, for example, in different phases of gas, liquid, and solid, and they might require completely different atmospheric conditions in order to obtain information about them. That is why different methods are optimised for different kinds of samples. The methods can vary from chemical methods, such as combustion analysis or titration, to different kinds of physical methods, such as various methods of optical spectroscopy. Sometimes a determination of concentration requires to combine these different methods.

The choice of method also depends on what information is needed from the sample. Collecting information about hydrogen, nitrogen and carbon, which is the element of interest in this work, falls in the research field of organic chemistry. Therefore natural starting point with measuring hydrogen, nitrogen or carbon is to look for the standard measurement methods in that field. Quantitative information about these elements is commonly obtained using combustion analysis. Combustion analysis refers to collection of methods, where the sample is burned under controlled environment and the analysis is done to the product of the combustion. This analysis can be done e.g. using optical methods such as non-dispersive infrared spectroscopy. Combustion analysis can sometimes reveal quantitative information about multiple elements from a single measurement.

While the combustion analysis has become a standard method for determining the concentrations for carbon, hydrogen and nitrogen, it is not applicable in all circumstances [1]. First of all it requires a laboratory environment to house the large equipment such as the kiln where the samples are burned and the machines used to standardise the samples. These include grinders and ovens for drying the samples. The preparation of the samples and the measurement arrangement can take very long time, especially because often the lab can not be located at the site where the samples originate from. This is the case for example in soil analysis.

When soil samples are collected from the location of interest, the samples need to be sent to a lab to be properly prepared for the combustion analysis. Since the preparation, such as drying, alone can take multiple days, this kind of analysis is obviously very time consuming. It is also hard to automatize due to the preparations of the samples and also the measurement device often requires calibration before each measurement set. In many applications this kind of drawbacks make the standard methods unfavorable. Such is the case for example in soil monitoring [2]. If we want to monitor carbon content of soil, we must have a method that can assess the carbon concentration as quickly as possible. For this purpose alternative methods must be considered.

Optical methods are often able to solve the issue of long measurement times [3]. As such, laser-induced breakdown spectroscopy (LIBS) is an attractive alternative to combustion. LIBS can be utilized on-site and no complicated sample preparation is needed. As multielemental method, it can provide information on the elemental composition of, in principle, any kind of sample. When calibrated properly, LIBS can be used for quantitative measurements in addition to qualitative ones.

The aim of this work is to test how a laboratory based LIBS setup can be calibrated to measure soil carbon concentrations from soil samples that were reference measured using combustion analysis. Before calibrating the setup, optimal measurement parameters for carbon assessment are determined and two different laser source wavelengths are compared. Also effects of soil moisture on the LIBS results is tested.

This thesis consists of seven chapter in addition to this one. In second chapter a motivation for soil carbon monitoring is given, and the topic of the thesis is examined further. In the third chapter,

different existing methods are introduced for soil carbon assessment, and motivation for using LIBS specifically, is given. Chapter four gives a general theoretical background necessary to understand, first of all, LIBS as a method, and secondly, to understand the standard means of analyzing LIBS data. Fifth chapter provides information about soils in general as well as how the soil samples are prepared for the measurements carried out throughout this thesis. Experimental arrangement is presented in chapter six. In chapter seven, the results and their analysis are discussed. Chapter eigth concludes this thesis and wraps up the results. Also future of the project is discussed in this chapter.

2 Climate change and soil

According to the Intergovernmental Panel on Climate Change (IPCC) [4], climate in a narrow sense is the statistical average and variability of weather events over a predefined time-span and place. The quantities of interest often include variables such as temperature, precipitation and wind and the relevant time scales vary from several months to millions of years. Climate in more wider sense is the current state of the climate system, which is defined by IPCC as a complex self-interacting system consisting of the atmosphere, the hydrosphere, the cryosphere, the land surface and the biosphere. In addition to interactions between the compartments themselves, external factors such as solar and volcanic activity and anthropogenic disturbances affect the climate.

2.1 Climate change

The climate has undergone unparalleled changes since the pre-industrial (1850 $\rightarrow$) times. The temperatures keep exceeding previous record values decade after decade, each one hotter than the average temperatures in the beginning of the industrial era. Human actions have warmed the the average temperatures by 0.8°C - 1.3°C with 66% - 100% likelihood range [4]. This is visualized in Figure 1. The main cause for the warming of the climate are the increasing greenhouse gas (GHG), mainly carbon dioxide (CO_2), methane (CH_4) and nitrous oxide (N_2O), concentrations in the atmosphere. Around 79 % of the anthropogenic GHG originate from of energy sector, industry, transport and building. The remaining $\sim$22 % is caused by the agriculture, forestry and other land use (AFOLU) [5]. In total, around 700 Pg of carbon has been released to the atmosphere during 1750 - 2019, of which around 41 % remains captured there [4]. Carbon emissions relased since the industrial revolution by the fossil fuel industry (270 Pg) are approximately twice as large as the emissions due to land use change and soil cultivation (136 Pg) during that time [6].

The amount of emissions caused by land-use can be redused, for example, by decreasing the amount of biomass burning, by reducing the mining of limestone (cement production is the largest of all industrial emitters [7]), by carrying out reforestation, by limiting deforestation and by applying novel cultivational methods to bind carbon into agricultural soils. Soils are a carbon pool of around 2300 Pg of which 1550 Pg is in the form of soil organic carbon (SOC) and the rest, 750 Pg, is in the form of soil inorganic carbon (SIC) [8]. In comparison, the size of atmospheric carbon pool size is around 600 PgC and the pool size for vegetation is around 450 Pg [4]. Soil carbon sequestration has the potential to offset as high as 15 % of the global GHG emissions [9].

2.2 Carbon cycle

One of the most important biogeochemical cycles is that of carbon. Three largest carbon storages from largest to smallest are oceans, land and the atmosphere. Carbon has an important role in the process of photosynthesis and photorespiration in the terrestrial compartments of the Earth system. It is stored in the atmosphere in the form of CO_2 where it is then captured by photosynthetic plants such as vascular plants, mosses and algae and other autotrophs which utilize inorganic chemosynthesis. During photosynthesis, part of the CO_2 captured from the atmosphere is converted, with the help of solar energy and minerals and water from the soil, to carbohydrates to be subsequently consumed by heterotrophs. Some amount of carbon is, however, always used by the autotrophs to perform cellular respiration. In this process the enzymes consume oxygen from the air in stead of CO_2 and then release CO_2. Plants become detritus either by dying themselves or through heterotrophs and then become food for decomposers such as fungi. Now through detritus, consumers or decomposers the carbon is again available for consumption of the autotrophs.

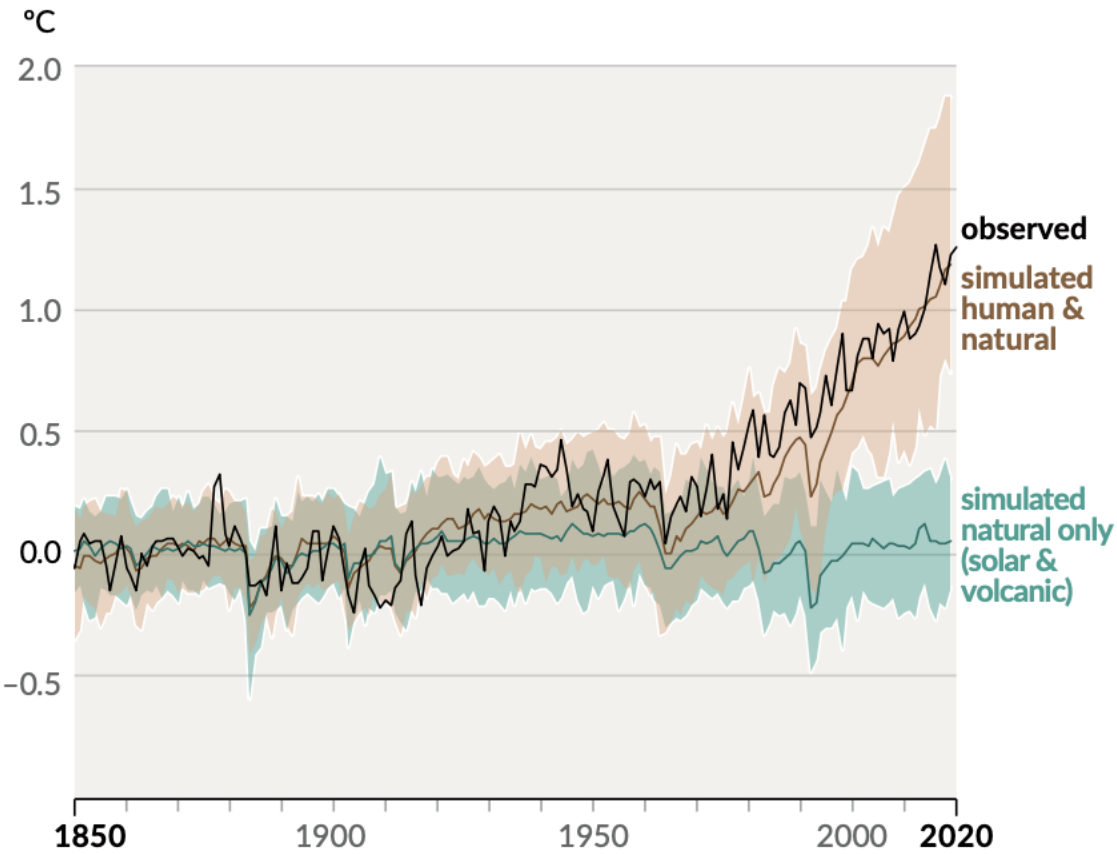

Figure 1. Temperature variation since the beginning of the industrial era with respect to time. The colored lines indicate average values from multiple models and the transparent colored regions show the 90-100% certainty region of the calculation. The black line is the observed temperature. Picture taken from [4].

Terrestrial gross primary product (GPP), when measured in the units of Pg of C/yr, is the measure of how much carbon is produced in photosynthesis in the ecosystem in a year. Around 50% of this carbon is released back to atmosphere through plant respiration. Often a measure of annual growth of terrestrial plants is defined as net primary product (NPP), which is defined as GPP - R_a, where R_a is the amount of carbon lost in respiration of autotrophs. Global values for GPP are estimated at around 120 PgC/yr and estimations for NPP are around 60 PgC/yr [10]. Further on, if the heterotrophic respiration R_h is taken into account and subtracted from the NPP value, an estimate for carbon stock is achieved. This value is often referred to as net ecosystem production (NEP), and it is defined as NPP - R_h. NEP values are often gained by measuring the difference between the incoming CO_2 flux from the atmosphere and the outgoing CO_2 flux from the ecosystem. Global annual NEP values peak at 10 PgC/yr but these numbers exclude the effects of forest fires and anthropogenic disturbances. When these are accounted for, the estimates for a net biome production (NBP) are steadily decreasing, i.e. less and less carbon is being sequestrated from the atmosphere each decade. Positive values imply carbon sinks whereas negative values imly carbon sources. In the 80's the values of NBP were around -0.2 ± 0.7 PgC/yr, in the 90's NBP was around -1.4 ± 0.7 PgC/yr.

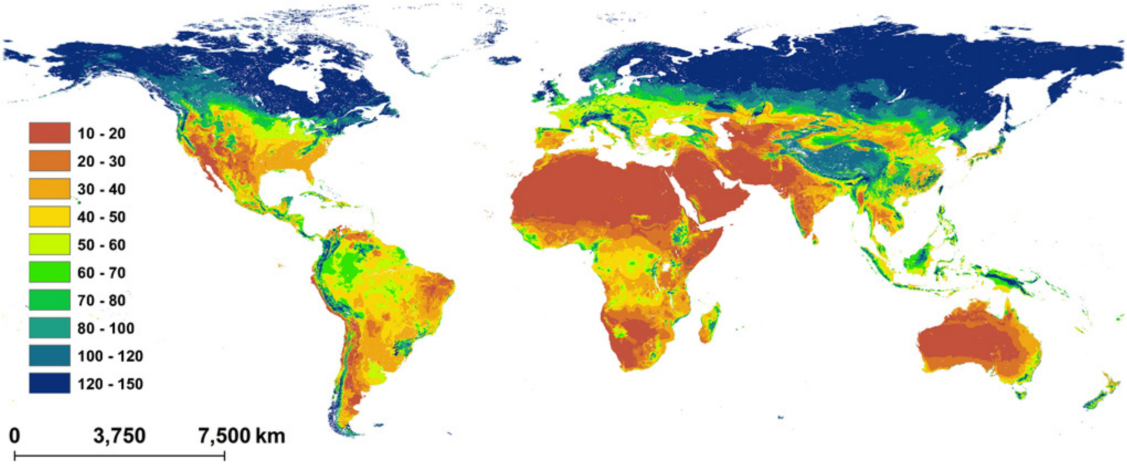

Figure 2. A map of global distribution of soil C stocks in topsoil (first 30 cm from the surface) in tonnes of C per hectare. Figure taken from [11] and generated based on global datasets of C stock from the study of [12].

2.3 Removal of carbon from the atmosphere by soil management

Considerable amounts of carbon can be removed from the atmosphere by changing the ways of land-use. Carbon can be sequestrated by more efficient crop and nutrient management, by changing the existing tillage methods, by more efficient irrigation and by changing the land cover. Also reshaping our practices on burning the land and crops helps reducing GHG emissions. Soil management practices that reduce CO_2 emissions also increase the SOC storage [13]. Cover crops are used to cover the soil to reduce erosion, which on it's own could cause major increase in the levels of released CO_2 [14]. Reforestration and afforestration can also play a significant role in increasing the terrestrial carbon sink. Potential of carbon sequestration by forest control is 0.4 PgC/yr where that of soil cultivation changes is 0.8 PgC/yr, so in total the land-use changes might be able to sequestrate 1.2 Pg of carbon each year [9].

In addition to the environmental benefits, increasing the amount of soil organic carbon also provides agricultural benefits. It improves soil aggregation, enhances biomass production, purifies both surface and ground waters while reducing the rate of enrichment of atmospheric CO_2 by offsetting emissons from the major sources, i.e. fossil fuels [6]. If the land area of Earth is taken to be 149 million km^2, it means that there are 161 tonnes of SOC in one hectare [11]. In reality, however, the SOC is not evenly distributed and best areas to increase SOC content are the degraded lands, since then it is possible to achieve offsets in GHG emissions while also improving the soil conditions. Most potential sites to increase SOC are agricultural lands which are estimated to be between 480 to 790 Gt C. At certain point soils also reach a point of equilibrium in the C content. Regions where SOC content is already relatively high (see Fig. 2), it might be that the equilibrium has already been achieved and it is difficult to increase the C levels any further.

Relatively small increases in the soil carbon stocks can have a significant impact on GHG mitigation, since soil stores up to three times more carbon compared to the atmosphere. Policy makers have created different platforms to subsidise the carbon sequestration methods. There is an agreement amongst scientists on the importance of incentivising the new agricultural methods to mitigate GHG while improving soil quality. The fossil carbon based GHG emissions are estimated at 8.9 Gt a year while the estimate for C stock of soil is 2400 Gt [15]. This means that in order to offsett the fossil CO_2 emissions, a 8.9 / 2400 = 0.4% increase in the carbon stocks is needed each year. As a result of the Paris Climate Agreement, United Nations launced a program named 4 per 1000 in 2015 where UN-countries strive to increase the soil carbon capture by that 0.4% every year. European Union has planned to set soil carbon amount as one deciding factor in their agricultural subsidy system. In addition to 4 per 1000, also other platforms provide environmental

Table 1. General trends in management practices and their effects on SOC accumulation. It must be noted that in reality, the rates vary between different climatic conditions. Values taken as reported in [11].

Management practices	SOC accumulation rates (t of C ha^{-1} y^{-1})
Afforestation	~ 0.6
Conversion to pasture	~ 0.5
Organic amendments	~ 0.5
Residue incorporation	~ 0.35
No or reduced till	~ 0.3
Crop rotation	~ 0.2

and economical benefits. The Kyoto protocol [16] is the first international agreement to mitigate climate change by reduction of net GHG emissions. It recognized the co-benefits gained through management and enhancement of carbon sinks in forestry and agriculture. EU Soil Strategy for 2030 [1] underlines the importance of soil to the terrestrial biodiversity and to feed and filter drinking water for nearly 10 billion people by 2050. It states that the soil degradation is costing EU several tens of billion euros yearly. The strategy has an aim to achieve land-based carbon neutrality in the EU by 2035.

Techniques that facilitate the build-up of organic matter exist and many of them has been tested and reported in [11] [17]. Even though the rates of SOC accumulation depend on the climatic conditions, according to 4 per 1000 initiative there are trends of types of soil management changes and their SOC accumulation rates as can be seen from Table 1. Higher C sequestration potential can be found on croplands with lower initial SOC stock, meaning topsoils with ≤ 30 t of C ha^{-1}. Here the annual C sequestration can reach even 1-3% whereas the higher initial stock croplands are limited to 0.4%, or 4 per 1000. Also the time after the management practices had been applied was reseached and the data shows that within the first 5 years, sequestration rates can be up to 2%, while after 20 years it reduces to 10% and finally after 40 years down to 0.4% as the SOC stock slowly reaches an equilibrium.

Even though the total biophysical potential of carbon sequestration can not be reached according to Smith et al. [18], it is still possible to make a significant contribution to climate change mitigation by 2030. Irrespective of the climate change mitigation, restoration and improvement of SOC stocks is also necessary for world food security making it a win-win strategy for the short period of 20 to 50 years [9]. Increasing carbon in soils helps to have better water infiltration and also has potental to increase agricultural productivity and ecological resilience [19]. However, there is no credible and reliable method of measurement/monitoring to assess carbon sequestration potential, to increase the statistical confidence of soil carbon measurements and to verify the amounts of carbon in soils directly [2]. The state-of-the-art methods, that have become standards in many fields of soil research, often prove to be time consuming and require excessive amount of labour. This labor is manifested as sample collection and preparation, in the requirement of laboratory environment in order to complete the measurements and the lack of automation in the process. Sending the soil samples to a laboratory and waiting for the measurements to be done can take multiple days. Also the measurements based on CO_2 fluxes require setting up the measurement devices all over the field which might disrupt the farmers work on the fields. Also they require certain type of environment and conditions in order to provide enough statistical confidence [20]. In order to make the monitoring of the carbon stocks possible, faster and robust methods of carbon monitoring are needed.

[1] https://eur-lex.europa.eu/legal-content/EN/TXT/?uri=CELEX%3A52021DC0699

3 Measurement techniques to determine soil carbon concentration

Even though this thesis focuses on LIBS, here other techniques that are being used for the same purpose of soil carbon assessment are presented. The purpose is to understand the ways in which LIBS differs from these other methods. Different kinds of methods for measuring carbon content in soils are applicable in different circumstances. They can be harnessed based on whether there is interest in the carbon distribution over a certain area, depth profile of soil carbon, amount of soil organic carbon compared to soil inorganic carbon or absolute amount of carbon in a single sample of soil. Monitoring soil carbon is essential factor in adopting new cultivation methods for storing carbon in the agricultural soils, enhancing the fertility, soil biodiversity as well as reducing erosion and water pollution [17]. Monitoring requires fast, robust, mobile and versatile method to verify the amounts of carbon in the soils.

3.1 Infrared spectroscopy

Different optical measurements can be used to detect molecules by their different characteristic ways of oscillating. For example molecules in a gas usually rotate at a frequency corresponding to the microwave or far infrared (FIR) region (300 MHz - 300 GHz) of the electromagnetic spectrum. Molecular vibrations on the other hand take place in the infrared region (300 GHz - 400 THz) [21]. Molecules couple to electromagnetic radiation and absorb photons when they are radiated at the characteristic frequency of the molecular oscillation.

Electromagnetic radiation with wavelengths longer than 100 µm (microwave region) is not energetic enough to cause drastic changes in the electron - not to mention nuclear - configuration of the atom or molecule it interacts with. It is able to change its orientation, which causes changes in the dipole moment of the molecule. For a molecule to have a dipole moment in the first place, it must be heteronuclear, since mononuclear molecules are formed by charged particles of similar polarity and hence they do not form effective electric dipoles. Dipole rotations can interact with an electric field by absorption or emission of energy. Infrared spectroscopy refers to the use of electromagnetic radiation in the infrared region that causes vibrations in the molecular bonds of elements [3].

When measuring the transmission of the broadband infrared radiation that radiates the material, it is observed that at certain frequencies, not all light that enters the material enters the detector. This means that some of the photons entering the material are absorbed and scattered by molecules in it. Specifically, when an infrared photon with same energy as the energy difference between two adjacent vibrational energy states (adjacency resulting from the selection rules) of and electric dipole hits the dipole, it raises the vibrational energy state of the dipole from i to $i+1$ and hence the photon does not proceed to the detector. Then a drop in the broad transmission signal is observed at this frequency and because the drop happens exactly at the characteristic frequency of the dipole, the element that absorbed the photon can be identified. Now, it is customary in infrared spectroscopy to talk in units of wavenumbers k, $[k] = \text{cm}^{-1}$, instead of frequencies. These are related to each other by

$$k := \frac{1}{\lambda} = \frac{f}{v} = \frac{\omega}{2\pi v} \tag{1}$$

where λ is the wavelength of the radiation, typically in cm, f stands for frequency, ω stands for angular frequency and v is the speed of light in the medium [22].

Because CO_2 is heteronuclear molecule, it can be detected using infrared spectroscopy. Figure 3 presents the infrared spectrum of CO_2. The infrared transmittance or absorbance can be measured

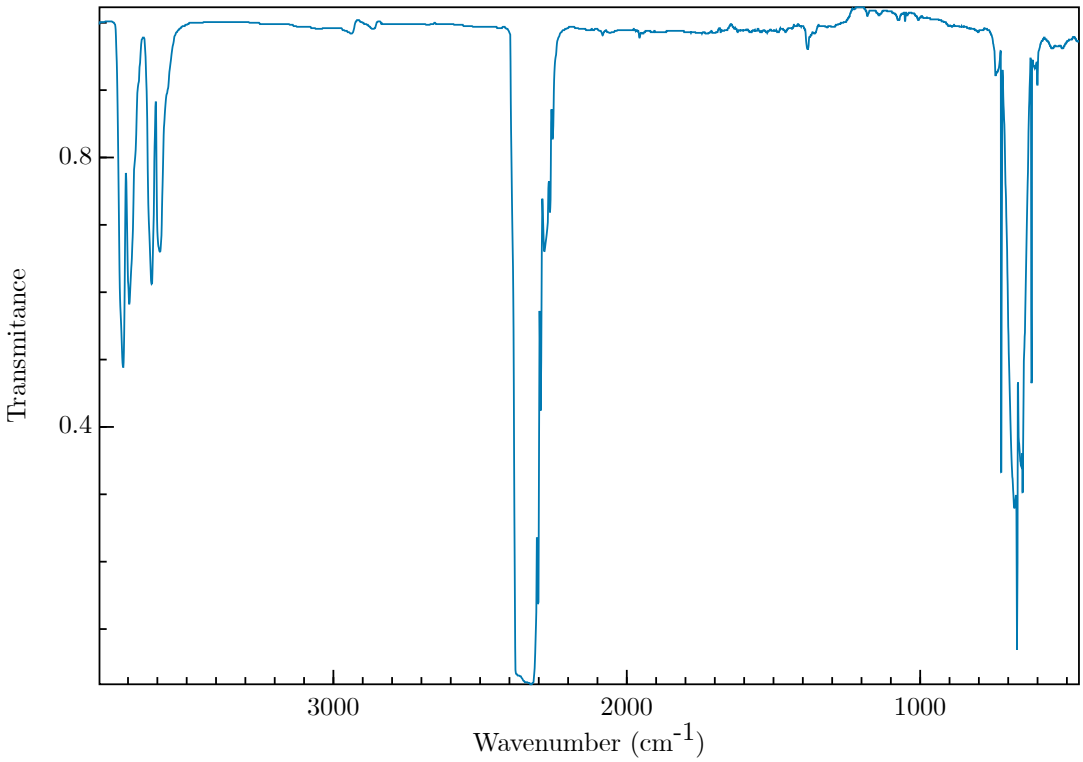

Figure 3. CO_2 infrared spectrum as transmittance with respect to wavenumber. Source: NIST Chemistry WebBook

e.g. using a traditional spectrograph or a nondispersive infrared (NDIR) sensor, that does not utilize a diffractive component such as a diffraction grating or a prism. NDIR sensors usually only detect a narrow band of infrared radiation varying from few dozens to few hundreds of nm and are desgned to measure only a certain region of the electromagnetic spectrum characteristic to a certain molecule. NDIR sensors are often used for gas detection and the measurement setting for NDIR type of sensing usually consists of a chamber, light source, sample gas and the NDIR sensor itself [21]. Since, in principle, the difference between the absorbed signal and the background is caused exactly by the molecules of the sample gas inserted in the chamber, it can be directly related to the amount of gas in the chamber.

In case sensing multiple elements or otherwise broad spectrum is necessary, Fourier-transform infrared (FTIR) spectrometer can be used. FTIR is based on Michelson interferometer where a source of light is split in two using a beamsplitter. Then the two beams of light are reflected back from mirrors at some distance from the beam splitter but one of the mirrors is moved along the beam direction. This causes the two beams to be out of phase when recombined at the beamsplitter. When the recombined beam is recorded, an interferogram with light signal being measured with respect to the mirror displacement is obtained. Then using the Fourier transform

$$g(k) = \frac{1}{\sqrt{2\pi}} \int_{-\infty}^{\infty} dx\, f(x) e^{-ikx}, \tag{2}$$

the transmittance spectrum g as a function of wavenumber k as presented in Figure 3 and the interferogram signal f as a function of the mirror displacement x can be related to each other. Making use of computationally fast algorithms, such as the fast Fourier transform (FFT), FTIR

provides a fast way to obtain a wide spectrum quickly [22].

In principle IR techniques can be used to measure any kind of samples. However, liquid and solid samples always require more sample preparation. Liquid samples are often handled by inserting small amount of the sample liquid between two salt windows. Salt windows are polished sodium chloride, which is transparent to the infrared radiation and hence does not interfere with the measurement. Solid samples usually need to be grinded into fine powder after which they are pressed into thin pellets. Before handling the samples themselves, a background signal is recorded by measuring an infrared transparent salt pellet, such as potassium bromide, which is first prepared using the same procedure. Then another pellet is pressed but this time a little bit of sample is mixed with the salt. Between each measurement the press and the grinder need to be carefully cleaned using e.g. chloroform and also dried so that no traces of the cleaning substance ends up mixing with the sample. Also the samples need to be completely dry in order for the grinding and pelletising to work.

3.2 Near-infrared spectroscopy

Mid-infrared (MIR) region corresponds to fundamental bands of molecular vibrations. Near-infrared (NIR) corresponds to overtones and combinations of the fundamental bands [23]. This means that it is often much more cumbersome to analyze a NIR spectrum compared to that of the MIR one. On the other hand MIR often requires more extensive sample handling to optimise the signal and the measurements rely on reflectance. Owing to having smaller absorption coefficient in the NIR region of the spectrum, light is able to penetrate the sample and in general not much sample handling is required compared to the MIR methods. Since one of the main goals is to create a measurement technique ready for field measurements, this makes NIR much more appealing for measuring soil carbon. To get to the actual concentrations from a NIR spectrum, calibration models are needed. Due to e.g. the weak and mixed signal of NIR, the instabilities in the models need to be compensated, and for this, it is necessary to create as large and exhaustive calibration database as possible [23]. According to [24], NIR spectroscopy alone does not provide sufficient accuracy for the purposes of soil carbon sequestration, monitoring and verification. It can, however, be utilized e.g. to map soil carbon variability for more efficient sample collection.

3.3 Eddy covariance method

One way to estimate the intake of carbon by the soil is to compare the carbon dioxide fluxes in and out of the soil. Carbon flux estimates are often computed using the eddy covariance method, where the vertical flows of air are measured to both directions and then the difference between the upward and downward CO_2 mixing ratios in the air flows are used as an indicator whether carbon is being stored to the soil or released to the atmosphere. The CO_2 flows are measured through a device consisting of an NDIR sensor based gas analyser for molecular classification and an ultrasonic anemometer for wind speed measurements. The flux is then defined as

$$F = \overline{\rho}_a \times \overline{w'\kappa'} \tag{3}$$

where ρ_a is the density of air, w is the vertical wind speed and κ is the mixing ratio for the element of interest, e.g. carbon defined by $\kappa := \rho_e/\rho_a$ where ρ_e is the density of the element of interest [20]. The overlines denote average values and the primed variables refer to the difference between the measured and the mean value, for example $w' = w - \overline{w}$ where w indicates the measured value for the vertical wind speed.

Eddy covariance method is utilized world-wide for CO_2 flux measurements. For example, the FLUXNET [2] program that monitorises CO_2 fluxes across the globe uses mainly eddy covariance for the flux determination. Eddy covariance method works best for flat and homogeneous terrains when the atmospheric conditions are steady [20]. When there is deviation from the ideal conditions,

[2] https://fluxnet.org/

compensatory methods are needed for a reliable signal. Eddy covariance method requires also setting up the flux towers, which might interfere with the farmers work on the field.

3.4 Elemental determination by combustion

The problems of measuring solid samples using IR methods described above can be managed by evaporating the solid samples into gaseous state for which IR spectroscopy provides reliable methods for measurement. Combustional element characterization has become a laboratory standard for a lot of different demands. It requires a separate laboratory to house a kiln that needs to be heated to near 1000 °C temperatures. Before the soil samples can be burned, they need to be sieved, grinded and dried which usually takes several hours or even days depending on the circumstances. After that the kiln itself needs to be calibrated by running multiple empty measurements and then by using some calibration samples such as the ethylenediaminetetraacetic acid (EDTA). Then small amounts, 250 mg, of sample such as soil are weighted and combusted and the measurements are repeated multiple times for accurate determination through averaging. When the sample is burned, the gaseous form can again be measured using NDIR detection. Without increasing too much the complexity of the system, the NDIR sensors provide a very selective measurement meaning that one can only measure limited number of elements simultaneously [21]. Commercial devices such as LECO are often tuned to measure carbon, nitrogen and/or sulphur (S).

3.5 Inductively coupled plasma atomic emission spectrometry

Atomic emission spectroscopy (AES) is based on the emission of photons when excited electrons return to lower lying energy states. In AES, the sample is vaporized and free atomic species of both ionic and neutral kind are produced. Then the atoms are excited and after some time they decay back to their ground states. When the electrons decay from higher energy states to lower ones, they release the excess energy in the form of a photon with energy that follows the relation $E = hf$ where h is the Planck constant and f is an electromagnetic frequency. The light emitted by a source can be analyzed using a spectrograph which diffracts the initial light into a spectrum of different frequencies or wavelengths. Using the emission spectrum, the characteristic wavelengths of elements can be identified for determination of concentrations, masses or e.g. some qualitative information about the sample.

Inductively coupled plasma-atomic emission spectrometry (ICP-AES) (sometimes also inductively coupled plasma-optical emission spectroscopy (ICP-OES)) is an example of an AES technique which utilizes radio frequency electromagnetic field to sustain a plasma initiated by a Tesla coil [25]. This plasma is then used to generate free atoms from a sample and to excite and ionize them. Common method to insert a sample to an inductively coupled plasma is to mix the sample in a solution and have it introduced to the measurement system in a continuous flow. The stream is guided to a nebulizer and mixed with gas which then converts the solution into aerosols. The aerosols are then filtered so that only the aerosols of appropriate size are guided to the plasma and rest are discarded.

The gas used in different phases of the measurement process can in principle be any gas, but common choice is to use noble gas due to its high ionization energy. This also yields a simple background spectrum thanks to the single atomic species of the gas, helping elemental characterization from the sample spectrum. Probably the most common choice of gas is Argon (Ar), mainly because of its availability and affordability and relatively high ionization energy of around 15.76 eV as demonstrated by Figure 4. Only elements that are beyond the ionization energy of Ar are helium (He), neon (Ne) and fluorine (F).

The sample aerosols are guided to the plasma torch inside a cocentric quartz tube of three layers. In the innermost tube, the sample aerosols are guided to the plasma, the intermediate tube is used to guide cooling Ar gas to the system and the outermost tube upkeeps the Ar gas flow to the plasma. The cooling is needed to keep the silicon (Si) tubes from melting due to the increase in current in the radio frequency generator. The radiative background of Ar gas is highest in the UV to VIS region peaking at around 450 nm, explaining the blue color of Ar ICP. Like all AES based devices, also ICP-AES measurement system need to be calibrated for each element before

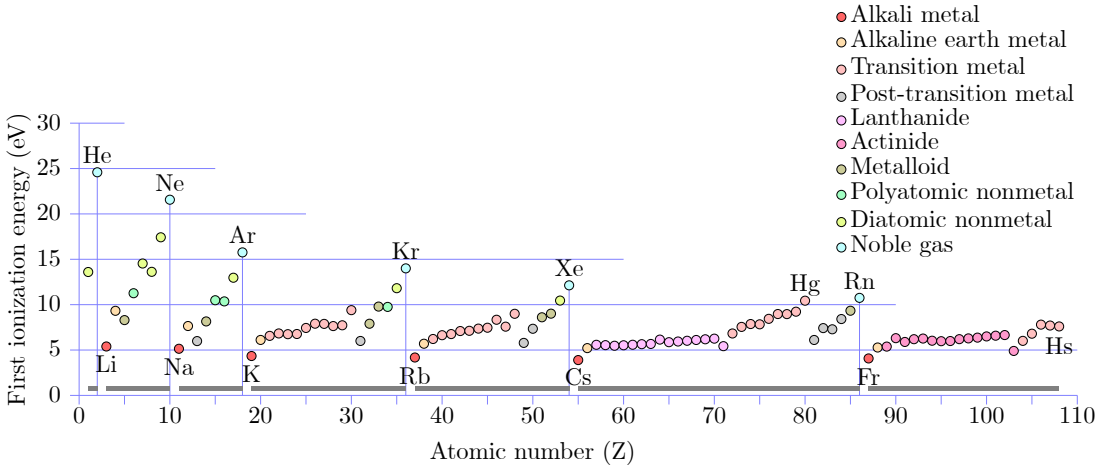

Figure 4. First ionization energies plotted against atomic number. As can be seen, the use of Ar as the gas source for plasma formation in ICP makes it possible to ionize all but three elements: helium (He), neon (Ne) and fluorine (F) that has an ionization energy slightly above the one of Ar. Source (CC BY 3.0)

quantitative determination. ICP-AES owns a favorable feature of being able to govern wide range of concentrations (up to four to six orders of magnitude). This means that the correspondence between the ICP-AES signal and a reference measured concentration follow a linear relationship until the self-absorption phenomenon at high concentrations [26]. Generally one can detect $\mathcal{O}$(ppb) concentrations using ICP-AES making it precise enough for multitudes of applications.

ICPs can also be used for mass spectrometry (ICP-MS). In mass spectrometry, inserted particles are accelerated to have the same energy. Then using an magnetic field created by an electromagnet, ions are sorted according to their mass-to-charge ratio. When combining with ICP, the ions created by the ICP torch are guided to the accelerator and analyzed after that. Since the measurement is based on mass evaluation, it is possible to distinguish isotopes using ICP-MS [25]. The detection limit of ICP-MS is $\mathcal{O}$(ppt), making it even more precise than the ICP-AES. This means that ICP-MS is able to measure concentrations of few nanograms per liter and therefore the whole measurement is extremely sensitive to contamination of the samples. Trustworthy results require the user of the technique to be experienced, since small errors can lead to false calibration of the method.

3.6 Laser-induced breakdown spectroscopy

Laser-induced breakdown spectroscopy is a semi-invasive AES based method for characterizing elemental compositions of materials. The basic setup for LIBS is presented in Figure 5 and consists of pulsed laser, focusing optics and light collection optics. The pulsed laser is shot at a focusing lens, whose focal point is on the surface of the target. When a laser beam energetic enough is focused on the surface of the sample, around 1 µm^3 portion of the sample is ablated, depending on the state of the matter of the sample. When the photons from the laser pulse keep irradiating the ablated material, it eventually ionizes the atoms and molecules resulting in free electrons. With ns laser pulses, the free electron density and temperature of the ablated material keep increasing and the ablated material forms plasma. The plasma plume then keeps absorbing the further incoming radiation, which means that the material is no longer being ablated. The plasma plume expands adiabatically until around 1 µs after the laser pulse [27]. The laser pulses used in LIBS are much shorter than the lifetime of the plasma plume and so, after the expansion, the plasma plume starts cooling down and the electrons return to the quantum states of the atoms and molecules from which they were decoupled from. Now electrons de-exciting atoms to lower lying energy states

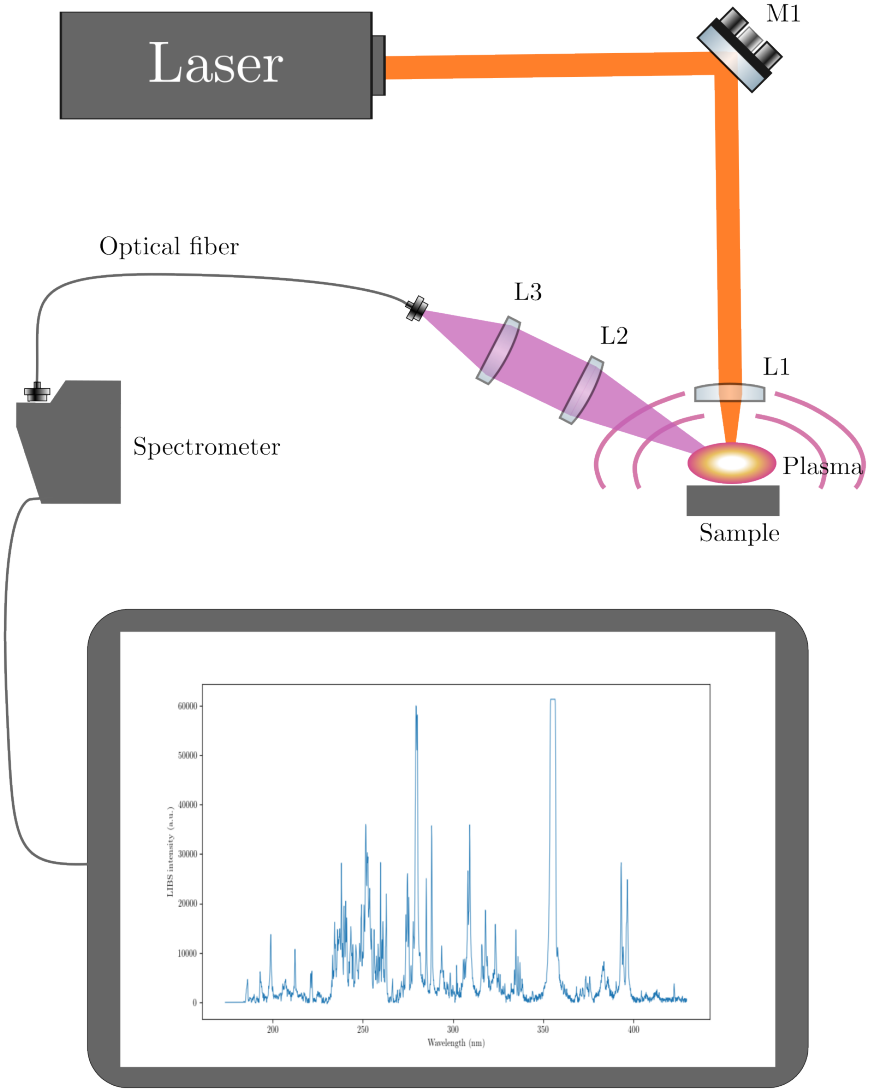

Figure 5. A schematic of a typical LIBS measurement. Laser beam is guided through a mirror M1 to the focusing lens L1 that then focuses the laser radiation to the surface of the sample. Then the cooling plasma is collected using lenses L2 and L3 into a optical fiber which guides the ligth to the spectrometer. A computer is then used to read the spectrum from the spectrometer.

cause a release of energy in the form of photons, which only radiate at the energies corresponding to the quantum energy states that the electrons excite to. Therefore, by measuring the radiation from the cooling plasma, and breaking it down into a spectrum of different wavelengths caused by different elemental transitions using e.g. a diffractive grating, it can be read from these wavelengths which elements were present in the sample [28].

The plasma formed in LIBS can be enchanced, i.e. its lifetime can be prolonged, its temperature and electron density raised etc., by several different methods. One possible method is to use

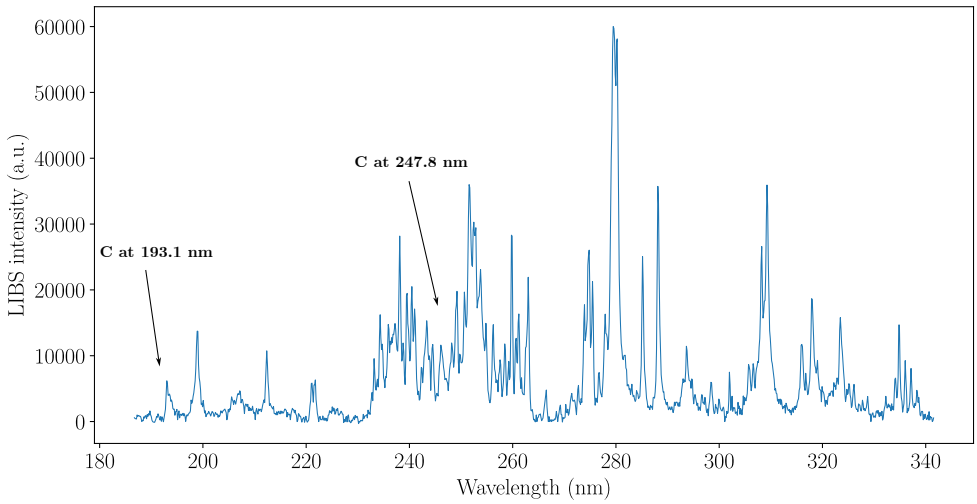

Figure 6. An example spectrum of plasma radiation intensity with respect to wavelength, and most commonly used carbon wavelengths marked using arrows. Both carbon peaks, the 193.1 nm one and 247.8 nm one, have been tested and used in soil carbon measurements, but in Finnish soils the 247.8 nm one is not resolved from the surrounding peaks of iron.

another laser pulse right after the ablation laser pulse ends to maintain the hot plasma for longer. Doing this, the laser energy couples more efficiently to the ablated material, usually resulting in signal enhancement and better limits of detection (LOD) [29]. Also maintaining the plasma using microwaves has been demonstrated to achieve the enhancement of LOD compared to regular LIBS. Even in atmospheric conditions nearly 100 fold improvement on the LIBS signal can be reached using microwaves [30].

LIBS can be used for both qualitative and quantitative analyses. When quantifying the concentration of a certain element from its LIBS signal, calibration is needed. This is usually done using a method of calibration curves. In this method the elemental concentrations are measured first with some other method and then the intensities of the elemental lines from LIBS are plotted against these reference concentrations. The method for reference measurements should be chosen to be one as precise as is the required precision for LIBS. In ideal conditions a linear response through origin is expected between the reference concentration and LIBS signal. This, however, is not always the case. The calibration curve is often divided in separate linear regions with different sensitivities. Different physical phenomena affect directly to the sensitivity. Some elements of the spectra are prone to broadening due to different reasons, e.g. Stark broadening, natural broadening and Doppler broadening. In the higher concentration region the loss of sensitivity is often caused by self-absorption. These physical effects are discussed in more detail in Section 4. Also the hardware affects the sensitivity. For example the resolution of the spectrometer determines which elemental lines can be distinguished from each other and when two or more lines are mixed at low resolution, the intensity of the LIBS signal is not reliable. Sometimes the detector might also be saturated which means that its response does not correspond to the true intensity of the elemental line.

Sometimes the sample under measurement might have a complex sample matrix which causes significant variation in the signal and therefore the intensities of spectral lines. Then a method of internal reference might be useful to linearise the relationship between the line intensity and the concentration. Internal reference can be an element in the sample that remains approximately constant in the varying matrix. For example in an agricultural site there might be pretty even vertical and horizontal distribution of elements such as silicon (Si) and aluminium (Al), which are second and third most abundant elements in Earth's crust and biota after oxygen (O) [31].

Therefore after measuring their concentrations, one should plot, not the intensities of not the original element of interest, but the ratio of that and the internal reference against the reference concentration of the element to achieve a linear relation between them. Then because to a certain precision the amount of the element used as an internal reference is known, calibration of the LIBS method can still be done according to this calibration curve.

LIBS is a simple method in principle and the different setups vary from laboratory setups to handheld devices. Handheld devices are often limited in the laser beam energy and because not all materials are as easily ablated as others, not all materials can be measured with these devices either. Metals and other materials with single electrons in higher energy bands are more keen to release them and therefore start the plasma formation. Same is not the case with e.g. soils or many other materials that require a lot more energy to begin the ablation. Due to the development in the components used in LIBS systems, the method at present day provides often sensitivity comparable or better compared to other field-deployable methods.

While LIBS as a method is robust, compact and requires little or no sample preparation, it also comes with its drawbacks. LIBS has generally poor limit of detection (LOD) and hard to calibrate. Poor sensitivity of LIBS can often be overcome by averaging over several pulses. This removes the effects of e.g. laser energy fluctuation or the pulse to pulse variation caused by sample inhomogeneities. Since typical frequenciess for pulsed lasers are $\mathcal{O}$(10 - 20 Hz) and commercial devices use lasers up to the kHz range [32], averaged measurement is still reasonably fast. LIBS has already been demonstrated for soil carbon measurements [33]. Carbon has its most prominent emission lines at around 193.1 nm and 247.8 nm. Research on soil carbon has been conducted using both of them and they have been compared in literature [1]. Cremers et. al. used in their [33] the 247.8 nm carbon line which was well resolved from the surroundign spectra. If soil sample from a typical Finnish soil is taken, the 247.8 nm line cannot be seen due to the interferring lines of iron (Fe) that is present in Finnish soils (see Figure 6) [34]. Regions therefore have effect on which methods can be applied for soil carbon determination. On some soils the 193.1 nm line might be overlapping with the nearby lines of aluminium. According to Senesi & Senesi [1] both lines proved good for evaluating C concentrations in unknown soil samples, the 193 nm line was more accurate on results in soils with low C content. Despite having already been demonstrated for soil carbon measurements, harnessing LIBS for soil carbon monitoring, along with investigating the calibration possibilities for soil carbon assessment, have not fully been studied.

4 Theoretical background of laser-induced breakdown spectroscopy

Here the basic principles behind the LIBS method are introduced. A general analytical description of a LIBS plasma is difficult. Many interactions between the plasma and the sample, plasma and laser, laser and sample and also e.g. interactions of plasma with itself need to be taken into account simultaneously. This is why the description is usually done instead using a thermodynamic approach.

4.1 Electromagnetic radiation

Electromagnetism is a unification of two forms of interaction, electric and magnetic, in terms of classical fields. The fields themselves are dependent on the medium and the most common way to mathematically couple the fields is through Maxwell's equations

$$\nabla \times \boldsymbol{E} = -\frac{\partial \boldsymbol{B}}{\partial t}, \tag{4}$$

$$\nabla \times \boldsymbol{H} = \boldsymbol{J} + \frac{\partial \boldsymbol{D}}{\partial t}, \tag{5}$$

$$\nabla \cdot \boldsymbol{D} = \rho, \tag{6}$$

$$\nabla \cdot \boldsymbol{B} = 0, \tag{7}$$

where $\boldsymbol{E}$ is the electric field, $\boldsymbol{B}$ is the magnetic flux density, $\boldsymbol{J}$ is the electric current density, $\boldsymbol{D}$ is the displacement field, $\boldsymbol{H}$ is the magnetic field and ρ is the electric charge density [35]. The fields $\boldsymbol{E}$ and $\boldsymbol{B}$ are general but the $\boldsymbol{D}$ and $\boldsymbol{H}$ depend on the medium where the fields propagate. These are connected by

$$\boldsymbol{D} = \epsilon \boldsymbol{E} \tag{8}$$

$$\boldsymbol{H} = \frac{1}{\mu}\boldsymbol{B}, \tag{9}$$

where ϵ and μ are the electric permittivity and magnetic susceptibility of the medium respectively. These quantities, $\boldsymbol{D}$ and $\boldsymbol{H}$ describe how the fundamental fields $\boldsymbol{E}$ and $\boldsymbol{B}$ interact with media, whether it is gas, liquid or solid. Now by looking at the curls of the curl-equations (4) and (5), the electric field and magnetic flux density are found to fulfill the wave-equations

$$\nabla^2 \boldsymbol{E} = \epsilon\mu \frac{\partial^2 \boldsymbol{E}}{\partial^2 t}, \tag{10}$$

$$\nabla^2 \boldsymbol{B} = \epsilon\mu \frac{\partial^2 \boldsymbol{B}}{\partial^2 t}. \tag{11}$$

Comparing these to the general wave equation of a general vector field $\boldsymbol{F}$

$$\nabla^2 \boldsymbol{F} = \frac{1}{v^2}\frac{\partial^2 \boldsymbol{F}}{\partial^2 t}, \tag{12}$$

where v is the velocity at which the field propagates at, it can be seen from (10) and (11) that the fields $\boldsymbol{E}$ and $\boldsymbol{B}$ propagate at speed

$$v = \frac{1}{\sqrt{\epsilon\mu}}. \tag{13}$$

In general let the waves propagate to a direction of vector $\boldsymbol{r}$. Then the general solutions to the wave equations (10) and (11) take the plane wave forms

$$\boldsymbol{E}(\boldsymbol{r},t) = \boldsymbol{E}_0 e^{i(\boldsymbol{k}\cdot\boldsymbol{r}-\omega t)} \quad \text{and} \quad \boldsymbol{B}(\boldsymbol{r},t) = \boldsymbol{B}_0 e^{i(\boldsymbol{k}\cdot\boldsymbol{r}-\omega t)}, \tag{14}$$

where $\boldsymbol{k}$ is the wavevector pointing to the direction of the propagation and ω is the angular frequency of the wave. Then using (14) it is noticed that

$$\nabla \times \boldsymbol{E} = i\boldsymbol{k} \times \boldsymbol{E} \quad \text{and} \quad \frac{\partial \boldsymbol{B}}{\partial t} = -i\omega \boldsymbol{B}. \tag{15}$$

Then the results above can be combined with (4) to get

$$\boldsymbol{k} \times \boldsymbol{E} = \omega \boldsymbol{B}. \tag{16}$$

Now taking the dot product with $\boldsymbol{E}$ both sides and using $\boldsymbol{E} \cdot (\boldsymbol{k} \times \boldsymbol{E}) = 0$ the result

$$\boldsymbol{E} \cdot \boldsymbol{B} = 0 \tag{17}$$

is obtained, i.e. it is seen that the fields $\boldsymbol{E}$ and $\boldsymbol{B}$ are always perpendicular to each other as well as to the direction of propagation.

From the definition of the Poynting vector

$$\boldsymbol{S} = \boldsymbol{E} \times \boldsymbol{H}, \tag{18}$$

it is seen that the units of $\boldsymbol{S}$ are $\mathrm{W/m^2}$ which gives the vector the interpretation of energy flux and since $\boldsymbol{E}$ and $\boldsymbol{H}$ are perpendicular to each other, the direction of the flux is the direction of propagation of the electric and magnetic flux fields. In other words, electric and magnetic field together form the electromagnetic field which carries energy in the form of electromagnetic radiation. The average of the length of the Poynting vector $S := |\boldsymbol{S}|$ represents the average power per unit are and is often called the intensity of the electromagnetic wave and denoted

$$I := \langle S \rangle_t = \epsilon v \langle |\boldsymbol{E}|^2 \rangle_t, \tag{19}$$

where $\langle \cdot \rangle_t$ denotes the time average of the variable $\cdot$.

4.2 Absorption and emission of light

Let us consider two energy stages of electrons in an atom or molecule E_i and E_j for which $E_i > E_j$. Then if an electron is occupying the higher state i and no energy is being put to the system, it is prone to decay from that level to, e.g. the lower level j. When this happens, the energy $E_{ij} = E_i - E_j$ is released in the form of a photon. This photon is related to an electromagnetic frequency by

$$f = \frac{E_{ij}}{h}, \tag{20}$$

where h is the Planck constant. If there are now atoms in lattice with some of them being in the state j, and there is a photon interacting with an atom in this state with energy

$$E_{ij} = hf, \tag{21}$$

there is a probability that an electron from the atom then undergoes a transition from the state j to the state i. Also, if the atom is initially at state i and photon with the same energy hits the atom, it has probability to undergo the transition from i to j. This time, however, at the final state there are in total two photons with the energy hf since the incoming photon adds to the emitting one. This type of transition is called stimulated emission. If the photon excites the atom from state j to the state i, the photon is said to be absorbed by the atom. When the transition

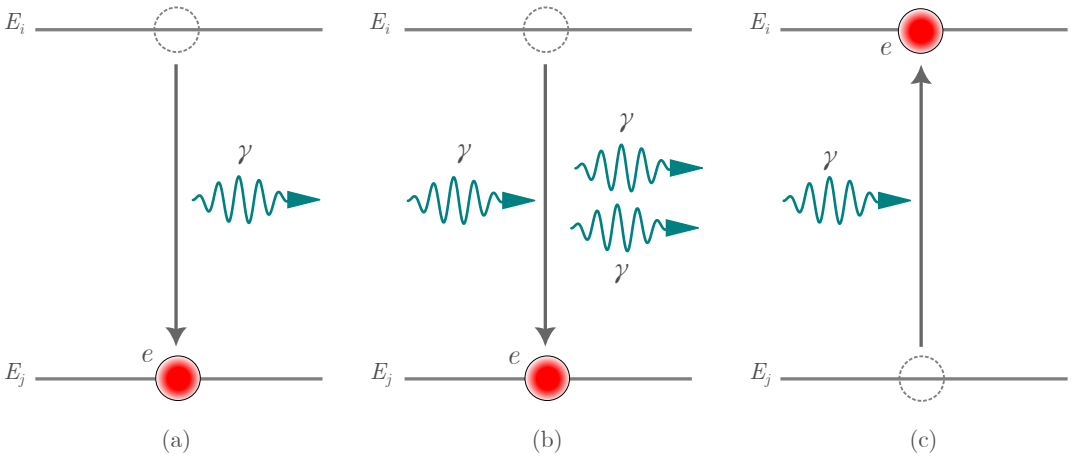

Figure 7. Schematic figure of emission and absorption processes in an atom. In (a), an electron originally at state E_i spontaneously decays to state E_j and this process is called spontaneous emission. In (b), an incoming photon stimulates the system causing the electron to decay from state E_i to the state E_j. The two photons in the final state of the interaction correspond to the incoming one and the one from the energy difference between the states. This process is called stimulated emission. In (c), an electron originally at state E_j absorbs a photon and excites to state E_i. This is called absorption.

from the higher state to the lower one happens without any external perturbation, the process is called spontaneous emission. These three processes are expressed in the Figure 7. For the purpose of LIBS, the most important type of change in the population of energy states is the spontaneous emission. Let us define population N of a state as the number of atoms in some volume in a certain state, for example in this case N_i is the number of atoms of the lattice in the state i. Now due to the spontaneous emission of photons, the population of that state in the lattice changes according to

$$\left(\frac{dN_i}{dt}\right) = -A_{ij}N_i, \tag{22}$$

where A_{ij} is the Einstein-coefficient of spontaneous emission. The dimension of A_{ij} is 1/s and it describes probability of photons of energy E_{ij} being emitted per second.

4.3 Laser radiation

Lasers radiate electromagnetic radiation that is characterized by being spatially and temporally coherent. Spatial coherence means that the radiation is directional, unlike classic sources of electromagnetic radiation. This allows the laser radiation to be guided and focused using optical components such as lenses and mirrors. Temporal coherence guarantees that the radiation is monochromatic, which means that it consists of only single frequency (or wavelength). The level of coherence varies and lasers can be built to produce very narrow or broadband radiation.

The flow of energy in the electromagnetic radiation is described by (19). In quantized theory, the energy of carried by the electromagnetic field consists of photons of discrete energies given by

$$E_\gamma = \frac{hv}{\lambda_\gamma} \tag{23}$$

where h is the Planck constant, v is the speed of light in the medium and λ_γ is the wavelength of

the electromagnetic field, related to the frequency of the field by (1) and again to the photon energy by (20). Now since laser radiation is monochromatic, an upper limit for the photon energy in laser radiation can be estimated using the vacuum value c for the speed of light and the laser wavelength for the photon electromagnetic wavelength λ_γ. The laser used throughout this thesis was a pulsed Nd:YAG (neodymium-doped yttium aluminium garnet) laser at its fundamental wavelength of 1064 nm and its third harmonic wavelength of 355 nm. According to (23), shorter wavelength photons carry more energy, and the energy carried by 355 nm photons is

$$E_\gamma = \frac{hc}{355.0\,\mathrm{nm}} = 3.493\,\mathrm{eV}. \tag{24}$$

4.4 Laser-induced plasmas

Let us now consider a solid sample that is being radiated using a laser. The sample can be thought of as a lattice of atoms and molecules. Bonding energies of atoms and molecules in the lattice are usually in the order of few eV. Even if shorter wavelength laser is being used, the energies required to change the structure of the lattice are usually not achieved. Below the bonding energies, thermal effects are dominant and in the time scale of $\mathcal{O}(10^{-15})$ s the photons interact with phonons in the lattice and the energy is transferred to heat. When, however, the lattice is heated enough or photon energies become higher than the bonding energies of the atoms, photon ionization, where photon excites electron to a high enough energy state for it to exceed the Coulomb attraction of the atom, becomes possible.

Ablation, i.e. the removal of atoms or molecules from the lattice, is required for the plasma formation [27]. Laser light couples to the material through the electric field as seen from (19) which causes the mass to leave in the from of electrons, ions, atoms, molecules and particles. For the ablation to happen, free electron generation is needed. Main ways for this to happen are multi-photon ionization and neutral atom collisions. In multi-photon ionization, multiple photons which may not be able to remove electrons from the atom on their own, hit an atom and remove one of its electrons, i.e.

$$X + n\gamma \rightarrow X^+ + e^-, \tag{25}$$

where n is the number of photons γ that interacted with the atom X. Then again if a free electron collides with a neutral atom with enough energy to remove one of its electrons, an excess electron is released

$$X + e^- \rightarrow X^+ + e^- + e^-. \tag{26}$$

This can cause a chain reaction when the end state free electrons hit yet other neutral atoms resulting in exponential free electron creation. When the free electrons ionize the material and the vapor further, a spark that is referred to as laser-induced plasma (LIP) is formed. During the early stages of plasma, the formation mechanisms and plasma properties depend highly on the irradiance and pulse duration of the laser. In a nanosecond regime, with irradiances of $\mathcal{O}(10^7)$ - $\mathcal{O}(10^{11})$ W/cm^2, the laser radiation will dominantly start the ablation by thermal mechanisms, by exciting the material and forcing it to undergo the phase transition from solid to liquid and from liquid to vapor. Then when the vaporized mass is being excited by the incoming laser radiation, after which it ionizes and forms plasma. This mainly occurs through a process of inverse Bremsstrahlung [36]. In Bremsstrahlung, a particle loses part of its energy in the form of a photon when its under the influence of an external electric field and so in the inverse process, the photon is being absobed by a particle in an external electric field. [37]

A complete description of LIP would be obtained by taking into account numerous different processes in the plasma simultaneously. Since this proves out to be extremely laborious, a thermodynamic approach is much more attractive [38]. Let us consider a general canonical thermodynamic system in an equilibrium. Multiple different distributions can be used to analyse different thermodynamical variables. In thermodynamic equilibrium the velocities $\boldsymbol{v}$ of the particles follow Maxwellian

distribution

$$f(\boldsymbol{v})\, d^3v = \left(\frac{m}{2\pi k_B T_M}\right)^{3/2} e^{-mv^2/2k_B T_M}\, d^3v, \tag{27}$$

where m is the mass of the particles, T_M is the thermodynamic temperature of the physical system and $v := |\boldsymbol{v}|$ is the speed of the particles. This is a probability distribution that is normalized so that integrating over all possible velocity values, the integral yields unity. Since the right hand side only depends on the inner product of the velocities $\boldsymbol{v} \cdot \boldsymbol{v} = v^2$, the direction of the particle plays no role in the probability. This means that all of the particles have the same probability of having a velocity $\boldsymbol{v}$. After the ablation and ionization processes the free electrons have relaxation time of $\mathcal{O}(\mathrm{ps})$ which means that the electrons in LIP attain the Maxwellian distribution of velocities in these time scales [39].

Another equilibrium distribution that particles follow is the Boltzmann distribution of population of energy states. With the classical partition function

$$Z_{\mathrm{Cl}}(T) = \sum_j e^{-E_j/k_B T} \tag{28}$$

the distribution is of the form

$$p_i = \frac{1}{Z_{\mathrm{Cl}}(T)} e^{-E_i/k_B T} \tag{29}$$

and it tells us the probability of the particle to be in the state i if its energy is E_i and the system is in temperature T. Intuitively, if a random particle was to be picked from the system, the probability for it to be a particle on the state i is n_i/n where n_i is the number (density) of particles in state i and n is the number of particles in the system in total. However, quantum mechanical effects need to be taken into account since the particles can also exist in multiple different spin states and so the probability has to be statistically weighted with the total number of different spin states $g_i = 2J + 1$ where J is the magnitude of the total spin vector, that is, the vector sum of angular momentum $\boldsymbol{L}$ and intrinsic spin $\boldsymbol{S}$, $\boldsymbol{J} = \boldsymbol{L} + \boldsymbol{S}$, of the particle in state i. Now the spin inclusive, quantum mechanical partition function becomes

$$Z(T) = \sum_j g_j e^{-E_j/k_B T} \tag{30}$$

and so the fraction of the number of particles in the state i compared to the total number of particles in the system n is

$$\frac{n_i}{n} = \frac{g_i}{Z(T_B)} e^{-E_i/k_B T_B}, \tag{31}$$

where T_B is the temperature of the physical system. The Boltzmann equation tells you the probability of finding a particle on a certain energy state. In a similar manner, the relative populations of different ionization stages of the same element are given by Saha-Eggert (sometimes just Saha) equation

$$\frac{n_e n_{\mathrm{II}}}{n_{\mathrm{I}}} = 2\frac{Z_{\mathrm{II}}(T_S)}{Z_{\mathrm{I}}(T_S)} \left(\frac{m_e k_B T_S}{2\pi\hbar^2}\right)^{3/2} e^{-(E_{\mathrm{ion}} - \Delta E_{\mathrm{ion}})/k_B T_S}, \tag{32}$$

where n_e is the electron density in the system, the subscript II denotes the variables of the ionized state and I denotes the variables of the neutral state, m_e is the mass of the electron, T_S is the temperature of the system, $\hbar$ is the reduced Planck's constant related to Planck's constant h by $h/(2\pi)$, E_{ion} is the ionization energy of the elemental species and ΔE_{ion} is the correction to the ionization energy due to Debye shielding [40]. In Debye shielding, the charged particles in the plasma cause other space charges to redistribute according to their polarization and therefore shield the charged particles from the effects of external electric fields. Debye length means the length at which Coulomb interaction has an effect in a certain medium, or in other words, it is the range of Debye shielding. Actually, Debye length is often used in the definition of plasma: in order for the

ionized gas to be called plasma, one requirement is that the Debye length is much smaller than the size of the plasma.

Finally, the distribution of spectral energy density for a single polarization is described by the Planck function [41]

$$B(f) = \frac{8\pi h f^3}{c^3}\left(e^{hf/k_B T_\gamma} - 1\right)^{-1}, \tag{33}$$

where f is the frequency of the photon, and T_γ is the temperature of the system. In thermodynamic equilibrium it is assumed that all of the equations (27), (31), (32) and (33) are coupled by the temperature, i.e.

$$T_M = T_B = T_S = T_\gamma. \tag{34}$$

This is not true in most laser-induced plasmas, since the plasma is generally optically thin and hence does not fulfill the condition of radiative equilibrium. In radiative equilibrium the optical thickness is required across the whole frequency range to achieve the black body spectrum. [38] That means that in LIP photon energies no longer follow the Planck distribution (33). If, however, the energy lost by radiation is smaller than the energy involved in other processes of the plasma, the Maxwell (27), Boltzmann (31) and Saha (32) distributions can still be assumed to hold. This kind of system is said to be in a Local Thermodynamic Equilibrium (LTE) and for the system

$$T_M = T_B = T_S \neq T_\gamma. \tag{35}$$

When LTE exists, the complex system of LIP can be thermodynamically described by three parameters: temperature, elecron number density and total number density of the species under interest. This is apparent from the discussion above: if LTE exists, the temperature of the system is fixed, and that fixes the thermodynamic equations (27), (31) and (32) so that they provide a meaningful description of the system. Therefore to justify the use of these distributions for plasma analysis and modelling, one wants a simple way to show that LTE is achieved. Most common way to do this is to obtain the temperature T and electron density n_e of the plasma and then show that they fulfill the so called McWhirter criterion [42]

$$n_e > 1.6 \times 10^{12}\sqrt{T}(E_{ij})^3. \tag{36}$$

This criterion is based on the assumption that the plasma is homogeneous and stationary [43], which laser-induced plasmas are not. This criterion of LTE is necessary but not sufficient. In addition, one should check that the temporal variations in both temperature and electron number density are small during the time it takes to reach excitation and ionization equilibria. Also the variation lengths of temperature and electron density should not exceed the distance travelled by a particle in diffusion during the relaxation time to equilibrium [38]. Because these last mentioned criteria are often very hard to check, it is not uncommon to find that LTE is often only assumed or justified by only showing that the McWhirter criterion (36) is fulfilled.

When doing quantitative analysis based on LIBS, three main assumptions are made by the plasma spark. Firstly, a stoichiometric ablation is assumed. Stoichiometry is based on the assumption of concervation of mass: quantities of products after a reaction relate to the quantities before the reaction. In the case of LIBS plasma it is assumed that the plasma plume emissions and the photon flux intensities received by the detector correlate to the quantities of elements in the ablated material. LIBS plasmas usually reach and exceed power densities of order 1 GW cm^{-2} and according to Chan and Russo [44], this is a limit value for the ablation to be stoichiometric. Non-stoichiometric ablation often happens at lower power densities, but the experimental parameters of LIBS can generally be selected so that stoichiometric ablation is guaranteed.

Secondly it is assumed that the plasma plume observed is in LTE as defined and described above. The lifetimes of excitations of different elements are much smaller than the lifetime of the plasma plume as a whole. If it is then assumed that during the lifetime of the plasma everything happens in LTE, the plasma can be described thermodynamically by Boltzmann (31) and Saha equations (32). These equations can be used to retrieve essential information from the spectral

data.

Thirdly the plasma plume is assumed to be optically thin so that photons entering the detector are resultant from any part of the plasma. If for some lines, the plasma is optically thick, the self-absorption effect will become apparent. In self-absorption the particle that emits a photon absorbs it back itself. This leads to widening and deformation of the spectral line which means that it is difficult to do any meaningful analysis using that line.

The time scale in which all of the mentioned effects happen from the multi-photon ionization to the initiation of the plasma spark is around the same order as the laser pulse in use, here that is $\mathcal{O}(\text{ns})$. It is salient to notice that the plasma parameters are dependent on the laser parameters such as wavelength, pulse duration and pulse energy. Since the plasma temperature and electron density define the plasma state, it must be kept in mind that different kind of lasers, namely the fs lasers, provide very different methods for forming a plasma. For example in the fs regime, non-thermal effects dominate the ablation and plasma formation and also due to the short pulse duration compared to the plasma lifetime, plasma shielding does not occur [45].

4.5 Spectral line shape and fitting

Electrons relaxing to lower lying energy states emit photons with frequency defined by (20). When measuring the emissions from the cooling plasma, the number of photons of certain frequency, or perhaps more commonly a certain wavelength that relates to the frequency by

$$\lambda = \frac{c}{f} \tag{37}$$

where c is the velocity of the photons, are measured. However, photons are never truly observed at an exact wavelength but rather spread around the certain wavelength as can be seen in Figure 8. Electrons return to lower energy states spontaneously in a plasma. That means the quantum states are not stationary and, therefore, they do not possess definite energies but rather a distribution of possible energies $E = hf$. This means that the spontaneously emitted photons have a distribution of possible frequencies f and also the spread in possible wavelengths λ is seen according to (37). This kind of line broadening is often referred to as natural broadening or radiative broadening and it results in lorentzian (sometimes also called Cauchy) function shape of the emission line defined by

$$L(x) = \frac{1}{\pi\Gamma\left[1 + \left(\frac{x-x_0}{\Gamma}\right)^2\right]}, \tag{38}$$

where $x_0 \in \mathbb{R}$ denotes the center of the function and Γ being the half-width at half-maximum of the function [46]. In general, when excited states are observed, they do not have infinite lifetime, and, therefore, the Heisenberg uncertainty principle

$$\Delta E \Delta t \geq \frac{\hbar}{2} \tag{39}$$

states that exact energies cannot be achieved, but instead the energies of the states always have variance. The natural broadening of emission lines is, however, usually very small in comparison to other broadening factors. A few important broadening factors include e.g. self absorption mentioned in the previous chapter, Doppler broadening and Stark broadening.

For a Doppler broadening, when an atom or a molecule is moving and one of its electrons emits a photon, an observer experiences a change to the frequency of the photon compared to a particle at rest, described by

$$f = f_0\left(1 + \frac{v}{c}\right) \tag{40}$$

where f_0 is the frequency when the photon emitting particle is at rest and v is the velocity of the emitting particle. This shift of frequencies of photons is collectively observed as broadening of the emission line and sometimes possibly a shift in the line as well. Instead of lorentzian shape, the

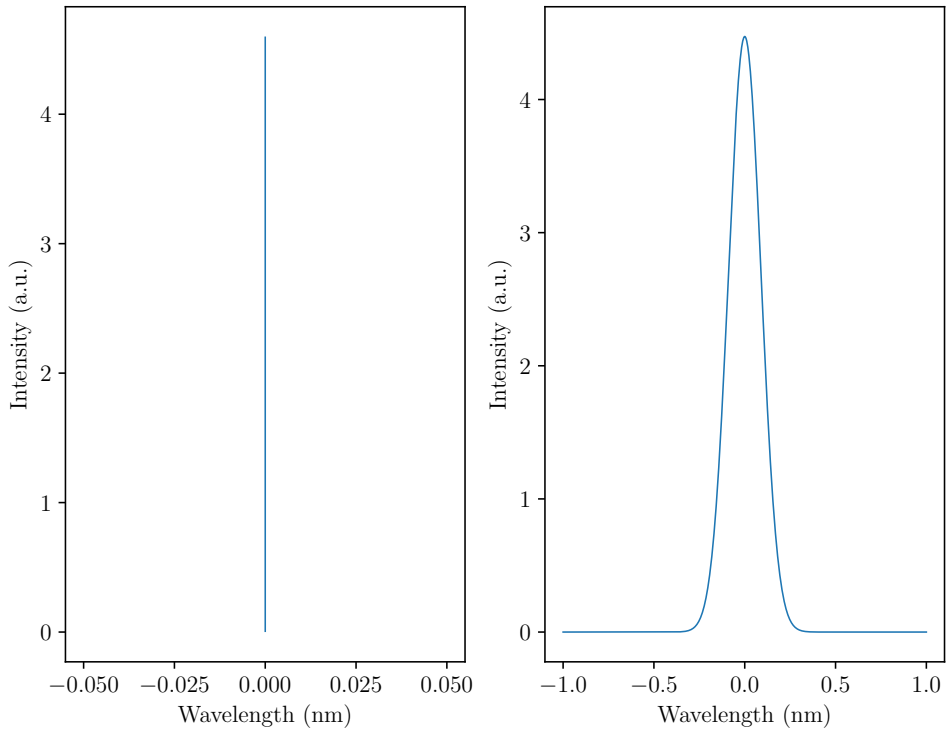

Figure 8. Two figures of emission intensity with respect to wavelength. On the right hand side is a line naturally broadened due to the uncertainty in the lifetimes of states. States are not stationary and hence do not possess definite energies. Energies are also limited by the Heisenberg uncertainty relation.

distribution in the Doppler broadening results in gaussian shape

$$G(x) = \frac{1}{\sigma\sqrt{2\pi}} e^{-(x-x_0)^2/2\sigma^2}, \tag{41}$$

with $x_0 \in \mathbb{R}$ denoting the center of the symmetric function and $\sigma \in \{\mathbb{R}|\sigma \neq 0\}$ being the standard deviation of the gaussian shape. The velocities of particles in the plasma under LTE follow the maxwellian distribution (27). Therefore some Doppler broadening is often observed in LIBS spectra when the particles move to different directions with different velocities with respect to the detector.

In the plasma plume, free electrons and ions of different electron configurations exist. When excited atom or a molecule experiences an external electric field, it affects its energy levels. The electron cloud distribution affects the energy that the electrons gain or lose from the external electric field and therefore the electron requires less or more energy to undergo the transition. This results in an effect called Stark effect, which is analoguous with the Zeeman effect where spectral lines get split due to spin-orbit coupling under an external magnetic field. Under the external electric field the energy states get split and sometimes the particle emits photons with less or sometimes with more energy compared to a particle that experiences no external electric field.

The width of a line is usually evaluated as the full width of the line at the point that equals half of the maximum of the line, or the full width at half maximum (FWHM). The Stark effect

causes the FWHM of an emission line to broaden by a factor [47]

$$\Delta\lambda_{\text{Stark}} = 2w\left(\frac{n_e}{10^{16}}\left[1 + 1.75A\left(\frac{n_e}{10^{16}}\right)^{\frac{1}{4}}\left(1 - BN_D^{-1/3}\right)\right]\right) \tag{42}$$

where w is the electron impact parameter, n_e is the electron density in the system, A is the ion broadening parameter, B is an coefficient equal to 1.2 or 0.75 for ionic or atomic lines, respectively, and N_D is the number of particles in a Debye sphere, a sphere which has the radius of the Debye length [37]. For purely lorentzian function the FWHM is

$$\Delta L = 2\Gamma \tag{43}$$

since Γ is the half width at the same point. For a gaussian shape, the FWHM is related to the standard deviation σ by

$$\Delta G = 2\sqrt{2\ln 2}\,\sigma, \tag{44}$$

where ln is the natural logarithm.

To obtain spectral line intensity from the experimental data, it is common to either take the maximum of the emission line as the intensity, or alternatively integrate over the line and use the area as the intensity. If the emission line of interest is well resolved and not mixed with any other nearby emission lines, the maximum of the emission line corresponds with the intensity of the emission. However, it might often happen that the emission line is partially mixed with some other elements emission line. Then the standard method is to fit a function to the emission line and integrate over the function for the intensity. Depending on the plasma properties, the best fit can be a gaussian function (41), lorentzian function (38) or a convolution of these two functions, known as the Voigt profile

$$V(x,\sigma,\Gamma) \coloneqq \int_{-\infty}^{\infty} dx'\, G(x',\sigma)L(x-x',\Gamma), \tag{45}$$

where σ is the standard deviation of the gaussian function and Γ is the half width at half maximum of the lorentzian function. Convolution like this calculates a moving average of two functions and hence the Voigt profile combines the behavior of both gaussian and lorentzian functions. This means that it provides a versatile fit to an emission line where both characteristic broadenings, gaussian and lorentzian, are present. Since the definition is not too practical for evaluating the function at points $x \in \mathbb{R}$, the values of the Voigt profile at x can be obtained from

$$V(x,\sigma,\Gamma) = \frac{\text{Re}\{w(z)\}}{\sigma\sqrt{2\pi}}, \tag{46}$$

where $w(z)$ is the Faddeeva function

$$w(z) \coloneqq e^{-z^2}(1 - \text{erf}\,(-iz)) = e^{-z^2}\left(1 + \frac{2i}{\sqrt{\pi}}\int_0^z dt\, e^{t^2}\right) \tag{47}$$

where erf stands for the error function, for a variable $z \in \mathbb{C}$ defined by

$$z \coloneqq \frac{x + i\Gamma}{\sigma\sqrt{2}}. \tag{48}$$

Figure 9 visualises the differences between equations (38), (41) and (46).

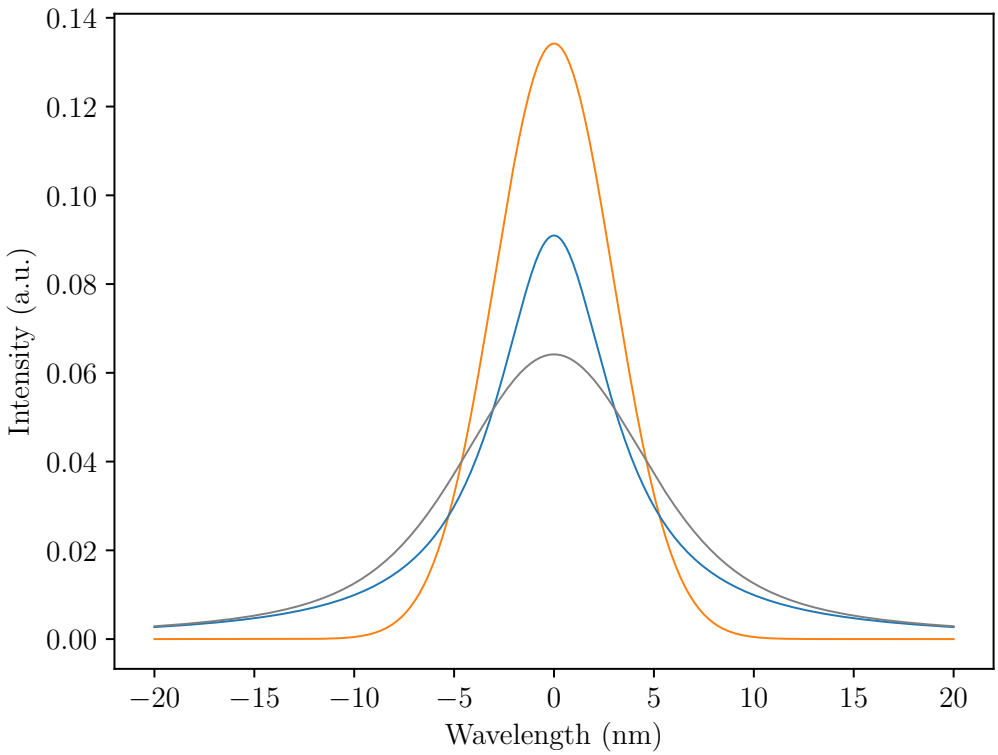

Figure 9. Gaussian and lorentzian functions with the same full width at half maximum. With gray color is drawn the convolution of the two functions, the Voigt function. The emission lines of elements are naturally widened to be gaussian shaped as a result of energy levels being smeared according to Heisenberg uncertainty principle. Gaussian shape originates from other sources of line broadening such as the Doppler broadening.

4.6 Electron density and plasma temperature

Intensity I_{ij} resulting from photons released from transition $i \to j$ in a LIBS measurement can be defined as the number of transitions reaching the detector in unit time and unit volume [47]

$$I_{ij} = n_i A_{ij}, \tag{49}$$

where n_i is the number density of electrons in state i as described in (31) and A_{ij} is the Einstein coefficient defined by (22) describing the rate of photons reaching the detector. Then using (49) to rewrite (31), the intensity becomes

$$I_{ij} = n \frac{A_{ij} g_i}{Z(T)} e^{-E_i/k_B T}, \tag{50}$$

where I_{ij} can be evaluated by integrating (using FORTRAN QUADPACK through Python library SciPy) over the appropriate function fitted on the emission line and the transition rate A_{ij} as well as the partition function $Z(T)$ can be obtained from the tables by NIST[3]. Now let us rewrite the

[3]https://www.nist.gov/pml/atomic-spectra-database

equation [48]

$$I_{ij} \coloneqq FC_e \frac{A_{ij} g_i}{Z(T)} e^{-E_i/k_B T}, \tag{51}$$

where C_e is the concentration of the element of the line and F is a constant to be determined from experiments and the product is to yield the total number density n as in (50). This definition allows us to write

$$\begin{cases} y \coloneqq \ln \dfrac{I_{ij}}{A_{ij} g_i} \\ x \coloneqq E_i \\ r \coloneqq -\dfrac{1}{k_B T} \\ C \coloneqq \ln \dfrac{C_e F}{Z(T)}. \end{cases} \tag{52}$$

It is worth noting that the units in (52) are to be understood as described in [49]. Now a linear equation is obtained

$$y = rx + C. \tag{53}$$

If multiple intensities of the same element on the same ionization stage are measured, a linear fit described by (53) can be used to calculate the plasma temperature from the slope r as

$$T = -\frac{1}{k_B r}. \tag{54}$$

This method of evaluating the plasma temperature is called the Boltzmann plot method [48]. The transition rates A_{ij} and spins J of states are obtained from the tables by NIST. Statistical weights are calculated from the spins using $g_j = 2J + 1$ where J is the total spin of the upper state of the transition.

When the plasma temperature and the intensity of an ionized state of the same element are known, the Saha distribution (32) can be used to calculate the electron density. First rewriting it again in terms of signal intensity (49) results in [47]

$$\frac{I_{ij}^{\mathrm{II}}}{I_{ij}^{\mathrm{I}}} = 2 \frac{(2\pi m_e k_B T)^{3/2}}{n_e h^3} \left(\frac{g_i^{\mathrm{II}} A_{ij}^{\mathrm{II}}}{g_i^{\mathrm{I}} A_{ij}^{\mathrm{I}}} \right) e^{-(E_{\mathrm{ion}} - \Delta E_{\mathrm{ion}} + E_i^{\mathrm{II}} - E_i^{\mathrm{I}})/k_B T} \tag{55}$$

and then solving for n_e results [50]

$$n_e = 2 \frac{(2\pi m_e k_B T)^{3/2}}{h^3} \left(\frac{I_{ij}^{\mathrm{I}} g_i^{\mathrm{II}} A_{ij}^{\mathrm{II}}}{I_{ij}^{\mathrm{II}} g_i^{\mathrm{I}} A_{ij}^{\mathrm{I}}} \right) e^{-(E_{\mathrm{ion}} - \Delta E_{\mathrm{ion}} + E_i^{\mathrm{II}} - E_i^{\mathrm{I}})/k_B T} \tag{56}$$

Another method for obtaining electron density is to solve it from the broadening of the elemental line. One example is to solve it from the FWHM of a line that has been broadened by the Stark effect (42). The Stark broadening is strongest on hydrogen-like atoms and the strong line of H at $\mathrm{H}_\alpha = 656.285$ nm is usually the one where the broadening is most clearly observed [51]. In the equation (42) of Stark broadening in case of hydrogen atoms, the ion broadening parameter can be ignored, which simplifies the equation to

$$\Delta\lambda_{\mathrm{Stark}} = 2w \left(\frac{n_e}{10^{16}} \right). \tag{57}$$

This form of Stark broadening is usually referred to as the linear Stark effect. This has also been tested on all other H lines $\mathrm{H}_\beta = 486.133$ nm, $\mathrm{H}_\gamma = 434.047$ nm and $\mathrm{H}_\delta = 410.174$ nm [40]. From

(57) the electron density can be solved as

$$n_e = \frac{\Delta\lambda_{\text{Stark}} 10^{16}}{2w}. \tag{58}$$

The electron impact parameters for different atoms are listed in [52]. Since the Stark effect is strong on the hydrogen line, it can be assumed that the total FWHM of the line is due to the linear stark effect, i.e. $\Delta\lambda_{\text{FWHM}} \approx \Delta\lambda_{\text{Stark}}$.

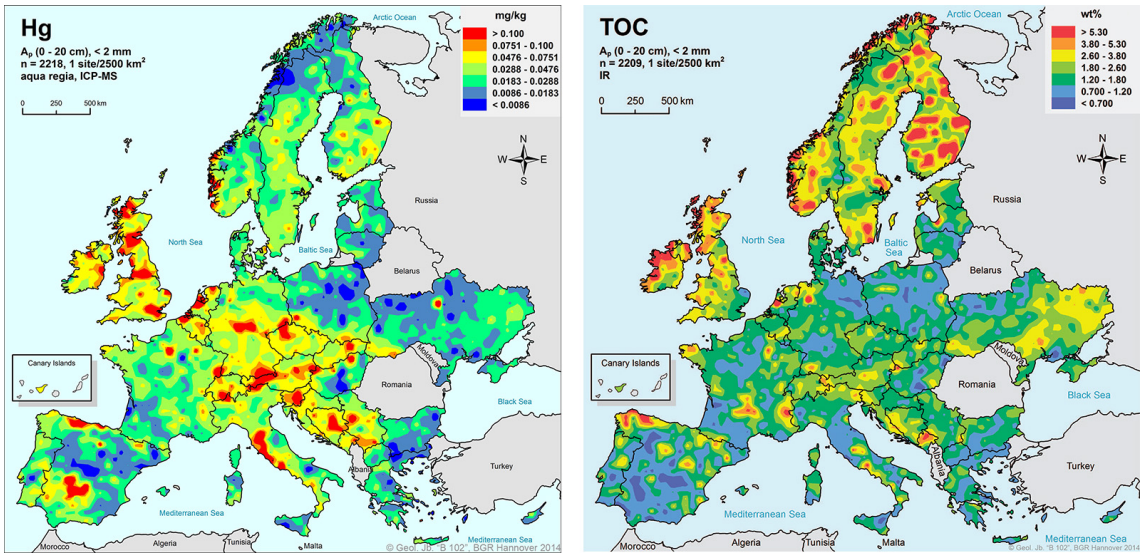

Figure 10. A map showing the distribution of Total Organic Carbon (TOC) across Europe. Finland, as well as other nordic countries, has particularly high concentrations of Carbon all across the country.

5 Soils and sample preparation

Basics of classification of soils and soil samples and their preparation are discussed here. Soils are a difficult sample matrix due to the wide spectrum of different elements they consist of and their naturally inhomogenic structure. Characterization of soils can vary regionally. However, certain unifying standards do exist and are used. Some experimental and analytical measures are needed to compensate for the difficulty of soil carbon assessment through a LIBS spectrum.

5.1 Characterization of soils

Soils are composed of particles of mineral and organic origin. Mineral particles are the result of degradated rocks, and organic particles originate from decaying plant matter and animal residues. In common classification systems used in Finland, sizes of the mineral particles determine the soil type. Two traditional methods for soil type classification, the RT-classification (rakennustekninen luokittelu) [53] and the GEO-classification (geotekninen luokittelu) [54], are explained on Table 2. When certain constituent particles of certain sizes are predominant over others, they determine the soil type.

Multiple different standards for soil characterisation exist. The classification mentioned above follows the ISO standard 14688 that is widely used in Finland [4]. One commonly used system for soil characterisation is the Unified Soil Classification System (USCS) developed by A. Casagrande. In this system the separation between coarse and fine is tested with a 0.074 mm sieve. If the grains pass the sieve, they are fine and if they remain in the sieve they are coarse. Then finer or looser sieves are used to classify soils even further. Also a textural classification system provided by United States Departmet of Agriculture (USDA) exists which takes more variables into account, such as soil moisture and temperature [55]. World Reference Base for Soil Resources (WRB) provides a

[4] https://www.iso.org/standard/66345.html

Table 2. Two common systems for classifying soils by their mineral particle sizes, RT and GEO. The Finnish name of the soil type is given in brackets after the translation to avoid discrepancies in the translated names.

RT system name	Mineral particle diameter (mm)	GEO system name
Boulder (lohkare)	> 1000	Boulder (lohkare)
Big rock (iso kivi)	between 60 and 1000	Rock (kivi)
Small rock (pieni kivi)	between 2.0 and 60	Gravel (sora)
Sand (hiekka)	between 0.2 and 2.0	Coarse and medium sand (karkea- ja keskihiekka)
Fine sand (karkea hieta)	between 0.06 and 0.2	Fine sand (hieno hiekka)
Finer fine sand (hieno hieta)	between 0.02 and 0.06	Coarse silt (karkea siltti)
Silt (hiesu)	between 0.002 and 0.02	Medium and fine silt (keski- ja hienosiltti)
Clay (savi)	< 0.002	Clay (savi)

systematic and extensive way of naming soils according to 202 qualifiers in total. Geological Survey of Finland (Geologian tutkimuskeskus, GTK) provides a map of the Finnish soil types according to RT and GEO systems [5]. GTK also provides a relation between RT, GEO and WRB classifications in [56].

Finnish soils are divided into mineral and organic soils where organic soils include soils such as peat and wetland soils, and are not treated in this thesis. Due to the plentiness of peaty and marshy arable lands, Finnish soils are also particularly rich in total organic carbon (TOC) as can be seen from Figure 10 [57]. These lands then further bind substances such as mercury or sulphur and hence cause regional anomalies in distribution of those elements [58]. Because of this sort of regional differences, many countries might have need for their own system of classification to match the requirements of the local environment.

In Finland, categorization into organic and mineral soils is based on their organic matter (OM) content and texture in the first 50 cm from the soil surface. If the soil has >20% of organic matter, the soil is organic soil and when the percentage is <20%, it is mineral soil. The mineral soils are then further classified as clay soils, silt soils, fine sand soils, sand soils and till soils according to the classification systems described earlier. Most of the land in Finland is covered by forests and around 8 percent of it is used in agriculture as can be read from Table 3[59]. In soil taxonomy (WRB), around 60 % of Finnish land is covered by Podzol, i.e. till that originates from moving glacial masses. Second largest area, 8%, is covered by Cambisols and the rest of it is Regosols, Gleysols and Lithosols. Most of the agriculture happens in the Cambisol lands. It must be noted that the classification of soils according to soil taxonomy is not unambiguous and therefore the Finnish soil classification might have been partially updated since the release of [59].

Samples used throughout this theses are gathered from two different agricultural sites in Finland, Qvidja, which can be seen from Figure 11, and ML, and they were provided by Carbon Action[6] partners. General information about the Carbon Action test fields can be found through the Field

Table 3. Finnish land use as of 1997 [59]. Other uses consists of e.g. the large open treeless areas in the very northern parts of Finland as well as open wetlands.

Land use	% of total area
Forests	68
Other uses	11
Inland waters	10
Agricultural land	8
Cities, municipalities, roads, etc.	3

[5] https://gtkdata.gtk.fi/Maankamara/index.html
[6] https://www.bsag.fi/carbon-action/

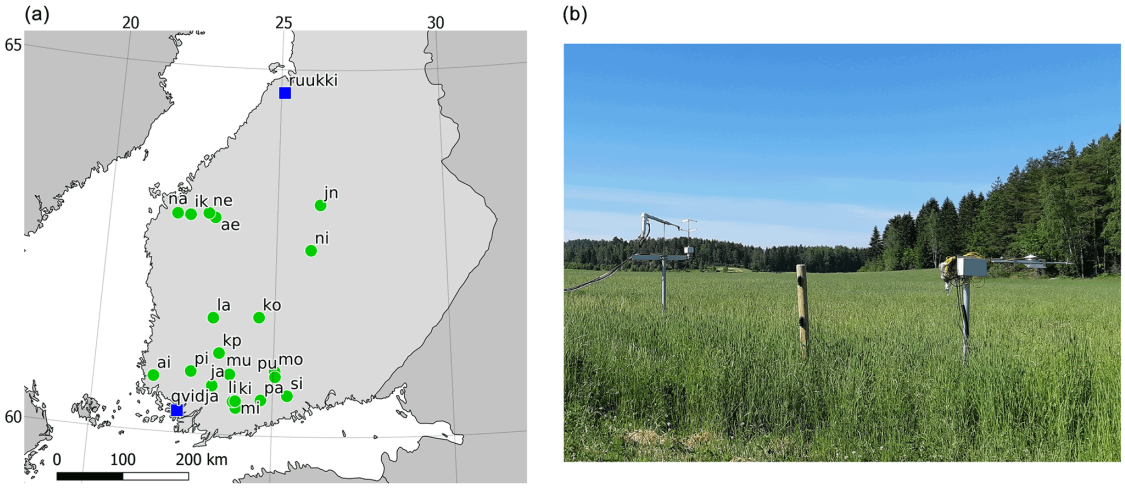

Figure 11. Advanced Carbon Action sites are marked on the map (a) with green dots and the intensive sites in Qvidja and Ruukki are marked with blue squares. On the figure (b) is presented eddy covariance tower and a radiation measurement instrumentation at the Qvidja intensive site. Image taken from [60].

Observatory [7] [60]. From both fields there were soil samples from depths ranging from the surface down to around 90 cm and the samples were collected from a single point of the field. Each soil sample was reference measured using dry combustion (LECO), which provides the concentrations of both carbon and nitrogen. Samples were therefore processed through the traditional sampling procedure of drying, sieving and grinding required by dry combustion.

Most prominent elements in soils include carbon, oxygen, hydrogen, sulphur (S), nitrogen, phosphorus (P), potassium (K), calcium (Ca), iron (Fe), silicon (Si), aluminium (Al), and magnesium (Mg). The first three are often present in higher concentrations. The three main elements in nutrition are N, P and K often referred to as NPK. Nitrogen is bound to soils in the form of nitrates which most often originate from the atmospheric nitrogen. Nitrogen is a key element in the growth of plants. Phosphorus aids energy transfer between different parts in plants and potassium helps plants to protect themselves from diseases. Calcium is related to the wellbeing of the roots of plants and magnesium is vital part of photosynthesis. In other words many of the common elements found in soils are from living origin such as plants and animals. Inorganic and anthropogenic sources such as breakdown of minerals and the use of fertilization introduce elements such as aluminium and silicon to the repertoire.

5.2 Sample preparation

The different organic and inorganic particles in varying sizes and the pores formed between the particles make the sample inhomogenous and difficult to measure reliably. Particle sizes, different sources of variation, including small stones, detritus from decaying plants, roots of plants and remnants from fertilizing and harvesting procedures, cause variation in LIBS shot-by-shot carbon intensity values. Even if the experimental parameters were otherwise well controlled, the sample matrix effects might result sequent plasmas being different from each other in temperature and electron density resulting in different LIBS intensities.

Even though these effects are somewhat inherent in the soils in any case, they can be toned down by sample treatment. This needs to be taken into account when designing the measurements themselves. For this reason, the samples in this thesis were pelletised with low pressure resulting in more homogeneous samples with a smooth surface. The pelletization requires a small amount of

[7] https://www.fieldobservatory.org/fi/online-field-data-fi/

purified (Milli-Q) water and therefore the samples needed also time to dry. After letting them dry overnight in room temperature, flat sample surface preferred by LIBS technique was achieved. It must be acknowledged that even with sieving and grinding the samples, some inhomogeneities will remain. For this reason it is also of great importance to diminish these effects by using greater amounts of spectra and then afterwards averaging over them.

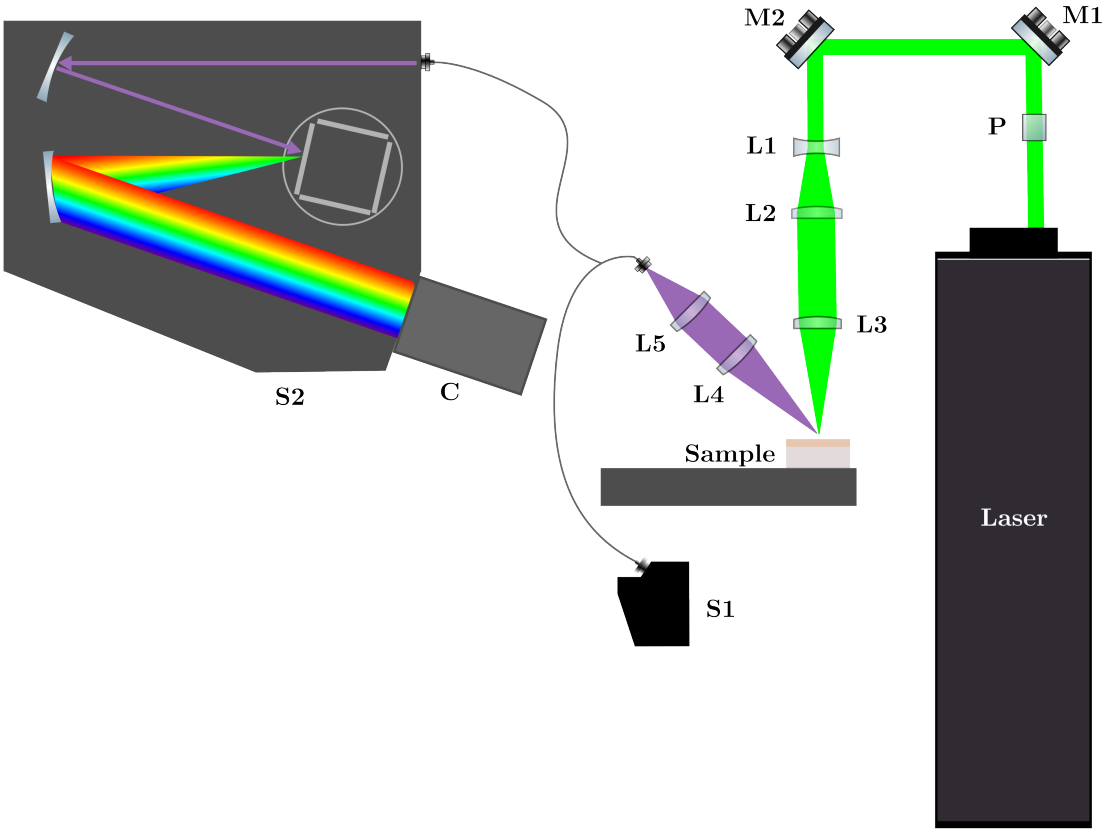

Figure 12. A schematic of the setup used throughout the thesis. The laser was a pulsed Nd:YAG 1064 nm with two frequency doublers making the use of 355 nm also possible. The mirrors M1 and M2 were 1064 nm coated mirrors, and when 355 nm was in use, the 355 nm coated ones were used. Lenses L1 (-50 mm) and L2 (200 mm) form a beam expander that expands the laser beam diameter four times larger to achieve better focus at the focusing lens L3 (50 mm). Two lenses collecting the light, L4 and L5, both had focal length of 50 mm. The collected light was focused on a bifurcated fiber bundle consisting of 19 fibers (200 µm diameter each) in the common end. Ten of the fibers were guided to the USB spectrometer S1 and the remaining nine were connected to the spectrograph S2. Spectrograph was connected to and ICCD camera C.

6 Experimental arrangement

In this chapter, the experimental arrangement and instrumentation are presented. All of the experimental arrangement focuses on the optimization of LIBS signal of carbon at 193.1 nm. Optimization in this case means that the parameters are adjusted so that the intensity of the carbon emission line is maximised.

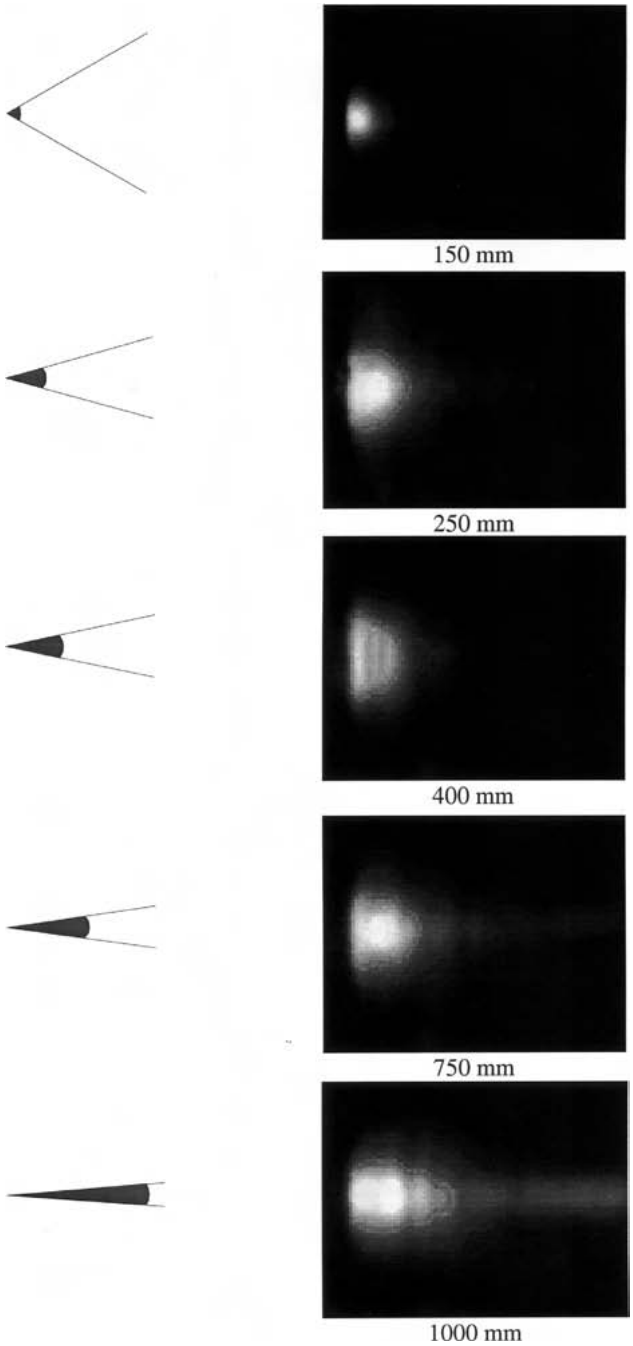

Figure 13. Figure to demonstrate how the focal cone shapes affect the shape of the plasma plume. On the left are presented the schematic focal cones. When longer focal length is used, the plasma forms more to the direction of the laser beam and hence might excite atoms from the surrounding air instead of the sample. Right hand side images are reconstructed from a measurement utilizing optical imaging. The Figure is taken from [61].

6.1 Instrumentation

A Q-switched Nd:YAG laser (Quantel Ultra) with its fundamental 1064 nm and the third harmonic 355 nm wavelengths was used for ablation of the samples. Q-switch is an attenuator in the optical resonator used to prevent lasing from beginning. Laser was used at 20 Hz repetition rate where the

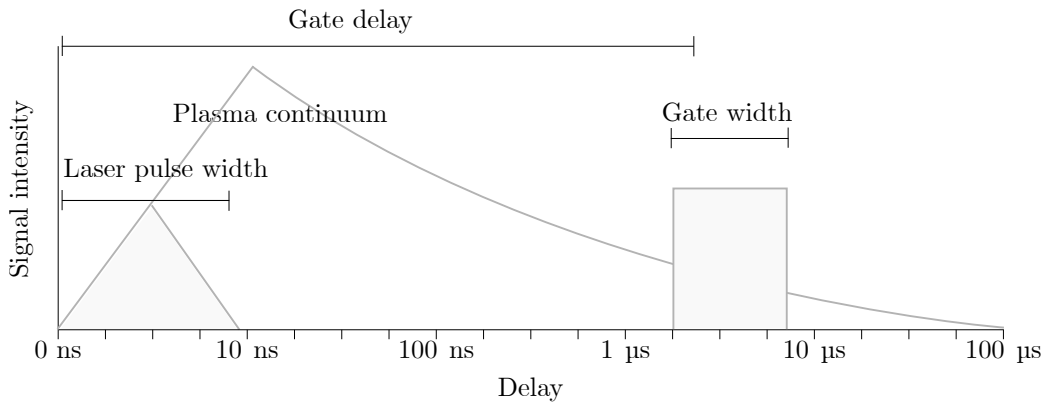

Figure 14. Schematic showing the approximate timings during the measurement. Logarithmic x-axis should be noted.

pulse duration was 8 ns. The beam was guided through two mirrors (depending on laser frequency NB1-K14 or NB1-K08, Thorlabs) and a few lenses before it arrives at the focusing lens as can be seen from Figure 12. First, the two mirrors, M1 and M2, were used to enable control over the laser beam path. Next a C-coated biconcave lens L1 (Thorlabs) with -50 mm focal lenght combined with a C-coated plano convex lens L2, (Thorlabs) with 200 mm focal length were used to widen the laser beam. By widening the laser beam, a tighter focal point can be achieved. The widened laser beam is then guided to a focusing lens which focuses the beam on a sample.

The focal length of 50 mm was chosen for the focusing lens L3 to achieve a shallow depth of focus as demonstrated by Figure 13. Then the plasma is formed on the surface of the sample and less elements in the elemental spectrum are resulting due to the plasma forming in air. Focusing the laser beam on a sample is usually done so that the focal point of the focusing lens is right below the sample surface. This also guarantees that the generated plasma plume is formed from particles from the ablated material and the effect of the surrounding atmosphere is minimal.

Radiation from the plasma plume was collected using a 75 mm plano-convex lens L4 with focal point inside the plasma. Then a similar lens L5 was used to focus the light inside an optical fiber that sequently guides the light to the two spectrometers. A bifurcated fiber bundle consisting of 19 multimode fibers was used for collecting the light. Each of the fibers were 105 µm in diameter and they were split so that other end has 9 fibers and the other has 10. An USB spectrometer S1 (Ibsen, FREEDOM UV-VIS) was used to record the near UV part of the spectrum from around 180 nm to 430 nm and a monochromator S2 (Andor, Kymera 328i) combined with an ICCD camera C (Andor iStar) were used to record spectra from above 600 nm. The Ibsen spectrometer is able to resolve the spectra with 0.3 nm precision. In the Kymera monochromator, different diffraction gratings are available. One with 1200 lines / mm was used. The spectral range of interest can also be varied from UV to IR by turning the grating system inside the device.

The laser head included two frequency doublers and was leaking some of the 532 nm green light even when only 1064 nm beam was supposed to exit the head. A polarising crystal was added in front of the laser head to filter out all the leaking radiation so that only 1064 nm or 355 nm were let through. The 532 nm and 1064 nm beams were perpendicular in their polarisation, so it was possible to block one of them without too much attenuating the other. This was done so that proper comparison between different wavelengths was possible.

Collecting the plasma radiation using a lens system as described in Figure 12, only a certain volume of the plasma is recorded. When the hottest and densest plasma is recorded, a lot more continuum is seen compared to recording some cooler region. The focal size of the collecting lens affects the maximal volume that can be recorded from the plasma at one time. The plasmas

produced by LIBS systems look something like the ones in Figure 13 where a clear, more bright, hot and dense center is seen as well as the cooler area surrounding it. If the fiber size is smaller than the plasma image, it is possible to scan different regions of the plasma.

6.2 Signal acquisition, delay, and energy control

The flashlamp of the laser was powered at rate of 20 Hz. Around 200 µs after the flashlamp, the Q-switch is turned off and the lasing begins. Laser pulse itself is being radiated almost immediately after the Q-switch opens, with delay of around 70 ns. The plasma formation begins in $\mathcal{O}$(ns) after the start of the laser pulse. It is not ideal to measure the formed plasma immeadiately after its formation, since the continuum caused by free electron bremsstrahlung dominates over the atomic emissions and nothing can be detected. This can also damage a sensitive ICCD camera if the light intensity and amplification is too high. Therefore a proper delay needs to be applied when carrying out measurements. This requires one to find out the internal delay that goes into all the electronics of the experimental arrangement. The spectrometers can be triggered straight from the laser Q-switch so that they start the measurement as fast as possible after the Q-switch is turned off. The trigger output of the Q-switch sends a voltage in form of a step function and the Ibsen spectrometer used in the measurements reacted to the descending edge of the Q-switch pulse. In order to start the measurements from the beginning of the Q-switch activation a function generator that generates a descending edge at the start of the Q-switch pulse is needed. This addition to the setup caused an additional delay of 362 ns to the system, which was verified using an oscilloscope.

The laser energy attenuation was controlled through a software. The energy of the laser pulse affects the ablation efficiency and, on the other hand, the temperature and electron density of the generated plasma. This means that when increasing the energy, different elements undergo different transitions, and an increase in the amount of the more energetic transitions is observed. This increase of the number of electrons on a certain elemental energy state can not go on forever since at some point there are no possible states for the electrons to transition to, and the energy saturates to a certain value. Increasing energy of the laser increases the intensity of the emitted radiation from the plasma. Sometimes the sensor of the spectrometer receives radiation of too high intensity, and the sensor saturates and can not display the intensities, like in the Figure 16 (a). If this happens while some important elemental data is still being improved by the increase of energy, this effect can be diminished by optically filtering the saturating wavelengths.

Table 4. Elements of interest, their corresponding wavelengths, and energy differences between the quantum states E_i and E_j. Number I indicates an atomic transition and number II an ionic one. Wavelengths taken from the NIST Atomic Spectra Database.

Element	Wavelength(nm)	E_j - E_i (eV)
Carbon I	193.1	1.3 - 7.7
Aluminium II	199.1	11.8 - 18.1
Silicon II	207.2	6.9 - 12.8
Silicon I	212.4	0.8 - 6.6
Silicon I	221.7	0.01 - 5.6
Silicon I	288.2	0.8 - 5.1
Hydrogen I	656.3	10.2 - 12.1

6.3 Elements of interest

The elemental lines in the spectra were identified using the NIST database. The elemental lines of interest and their corresponding wavelengths are tabulated in Table 4. Some of these lines were the result of transitions from a low lying energy state of an atom to the ground state. Some, particularly the lines of aluminium and silicon, were on the other hand ionic transitions. These elements were used as elements for internal reference when calibrating the LIBS setup. Also the ionic lines were used in the analysis of plasma temperature and electron density, since ionic transitions are required by the Saha equations (32).

For measuring the carbon intensity, the carbon line at around 193.1 nm was used. Right next to it there was an ionic line of aluminium but the spectrometers used in the measuremets had resolutions high enough to resolve the two lines. Atomic lines of aluminium at 198.0 nm and silicon at 212.40 nm were used for testing different calibration schemes for carbon. Hydrogen and carbon lines from 656 nm and 193 nm were used to follow signal properties when the amount of water in the samples was altered. Hydrogen line at 656.0 nm was particularly useful for determining moisture levels of the samples. As can be seen from Figure 24, when hydrogen peak was visible there was certainly moisture in the sample and it could be deduced that the carbon intensity was not at its maximum. In dry sample the hydrogen peak had disappeared completely.

7 Measurements

This chapter focuses on the measurements and the analysis of the results. Aim of the measurements was to find the optimal parameters for measuring carbon concentration, i.e. maximising the spectral signal of carbon at 193.03 nm. Optimal measurement parameters also help compensating the matrix effects of soils. Variables to consider include the timing variables (delay and gating time of the spectrometer), energy of the laser pulse and the wavelength of the laser source. To compare the wavelengths, all of the other optimisation measurements were performed two times: first by using the Nd:YAG laser at 1064 nm and second by using the third harmonic of the laser at 355 nm. First the dependency of carbon line intensity on the delay time was measured. After finding the optimal timing parameters, the energy was altered to see where carbon intensity reaches a maximum. These results were compared between the 1064 nm and 355 nm sources.

When optimal parameters were found, the calibration curves for two different field sample sets were measured. Here different elements were tested to function as the internal references for linearising the calibration curves. When curves for calibration were obtained, tests to remove some external deteriorating factors were performed. These include sample preparation and removing soil moisture effects by air drying the samples. The sample used in all of the timing and energy optimization measurements was from the Qvidja field, sample closest to the soil surface which includes around 2.7% of carbon.

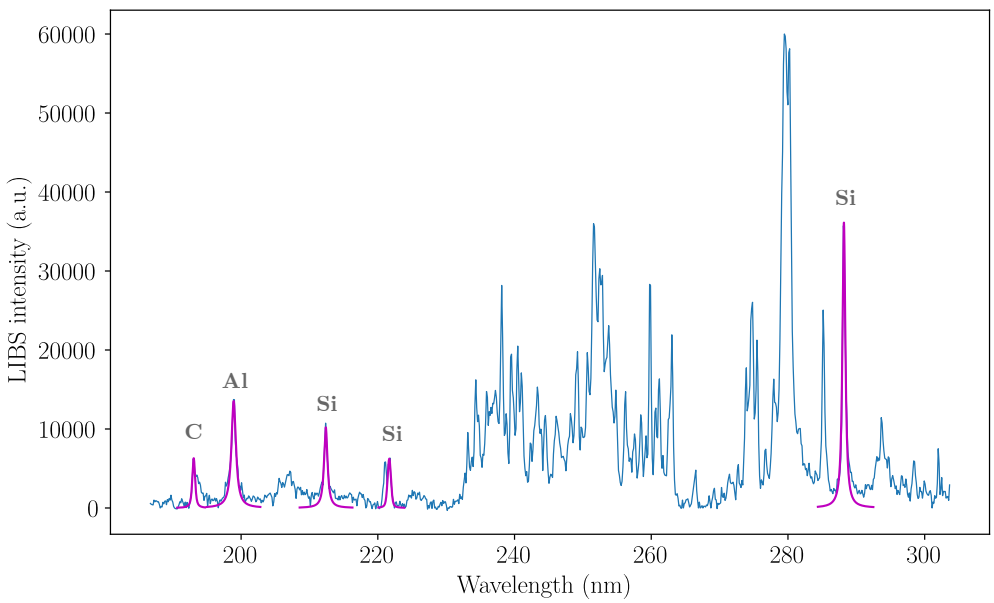

Figure 15. Example of a spectrum with Voigt function (46) fitted to the elemental lines of interest. All of the lines fitted here are atomic emission lines.

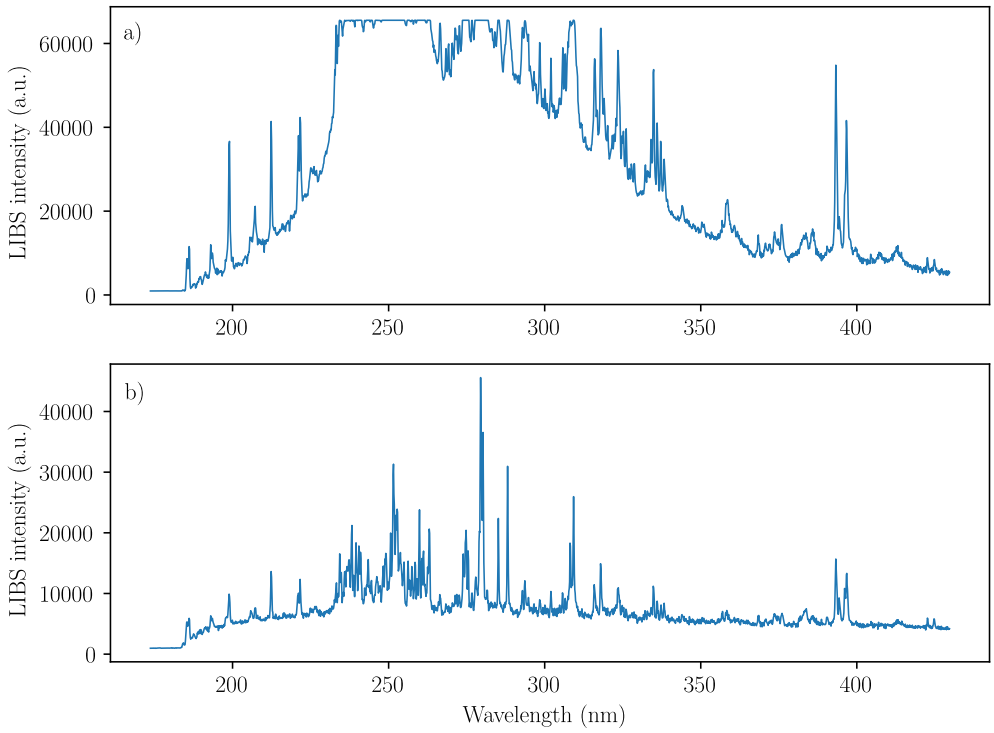

Figure 16. Figure of plasma radiation intensity with respect to wavelength using two different delay times. On the figure a), it is visible that broad emission continuum is still present in the spectrum. The figure b) is the same sample, but recorded 1.4 µs later than the a). The continuum disappears faster than the emission lines and they are seen resolved from the continuum.

7.1 Signal processing

All of the data analysed here was treated according to the following procedure: 100 separate spectra were collected after which the average of all of them was evaluated in a python code. Then the background was removed from the average spectrum using the rolling ball algorithm [62]. Then a Voigt profile (46) was fitted to the spectral lines of interest as seen in Figure 15 and the fit was integrated over in the Python program using techniques provided by the Fortran library QUADPACK [8]. These integrals were used as the intensities of the spectral lines in all of the measurements described in this section.

7.2 Optimal gate delay

To make sure that the correct temporal part of the plasma is being measured, the optimal delay still needed in addition to the total delay from the measurement arrangement described in section 6 needs to be found. First the gate width (time of exposure to light) was set from both spectrometers to 200 ns, which was the smallest step the USB spectrometer could be set to have. Then the delay was varied to make sure that a temporal region before the plasma reaches its hottest state was measured.

[8] https://docs.scipy.org/doc/scipy/reference/generated/scipy.integrate.quad.html

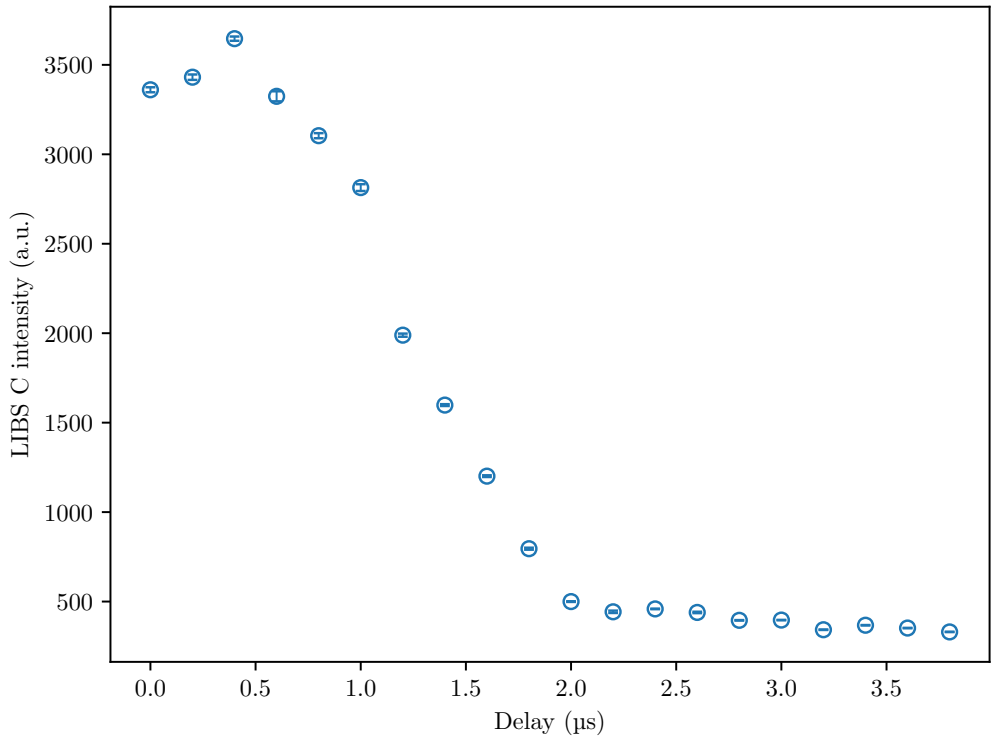

Figure 17. Carbon line intensity as a function of gate delay with 355 nm laser source. Delay is to be understood as the extra delay set from the spectrometer, excluding the global delay that originates from the setup itself. As expected, the values reach a maximum early on when the hottest instant of the plasma is measured and from there the intensities drop. The errorbars here show the standard deviation from the 100 intensities measured for each data point.

When measuring the earliest moments after the laser pulse, the plasma continuum is dominating wide range of the spectrum. This means that relatively early and hot stage of the plasma was measured, where the free electron bremsstrahlung dominates over the atomic emissions. These levels are often short lived and already after few hundreds of nanoseconds, the continuum has disappeared but lot of emission lines resulting from lower lying energy levels remain visible as can be seen from Figure 16. First parameter to optimise was the spectrometer delay to be set for both spectrometers. In other words, all of the delays mentioned here add to the global offset delay from the experimental setup. This was first done using the 355 nm laser source. Before varying the delay, the place of the gate window was verified. This was achieved by setting the gate width to the lowest possible value and varying the delay so that, first of all, the laser pulse itself is not being measured. Secondly, once certain that the measurements begin at a time when the laser pulse is gone, the gate width can be set to a longer value, such as 1.0 µs and start varying the delay. Starting from zero, the carbon line intensity as a function of delay can be read from Figure 17. With low delay values, the plasma as its temperature and electron density still increase is being measured. This can be seen as increase in intensity of the full spectrum. When the highest values of line intensity are reached, part of the intensity results from an offset or background in the whole spectrum caused by the continuum transitions. After a certain time the intensity values start to decrease due to the cooling of the plasma. In order to record the high intensity region the delay values of 600 ns were used. The exposure time is not as crucial of a variable as the delay itself,

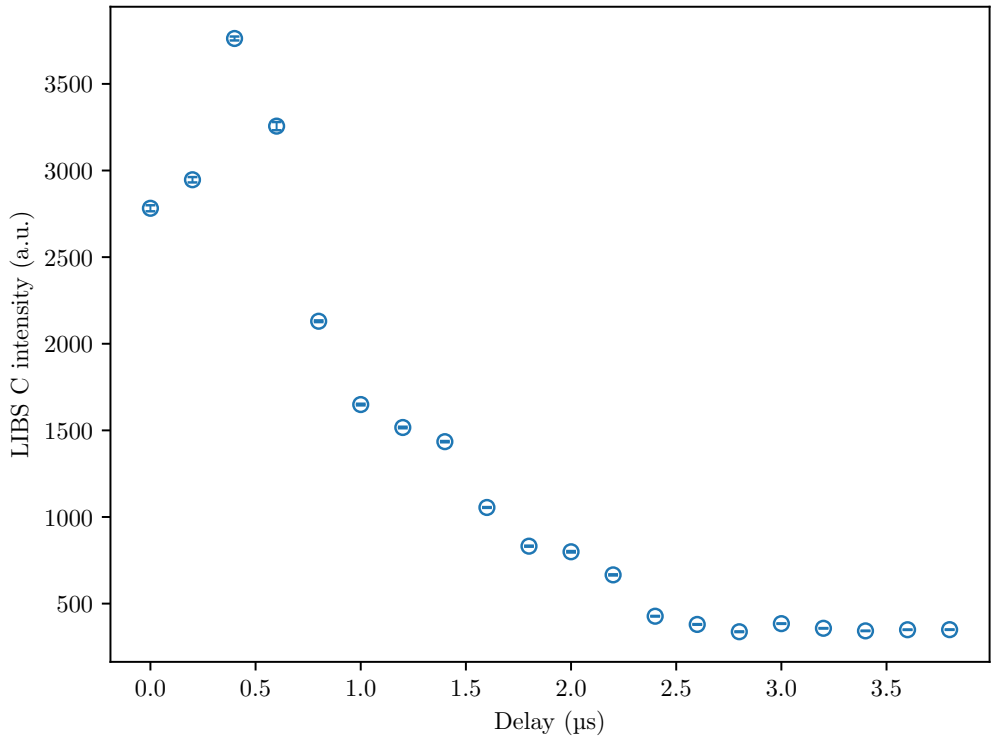

Figure 18. Carbon line intensity as a function of gate delay with 1064 nm laser source. Delay is to be understood as the extra delay set from the spectrometer, excluding the global delay that originates from the setup itself. As expected, the values reach a maximum early on when the hottest instant of the plasma is measured and from there the intensities drop. The errorbars here show the standard deviation from the 100 intensities measured for each data point.

since when the plasma is measured for a longer time, the added signal is approaching zero. One thing to take into account is that it is not set to be so long that the next laser pulse and plasma formation are being measured. From Figure 17 the optimal gate width is estimated to be around 1.2 µs, starting after the 600 ns delay.

Repeating the measurement but changing the laser source to the 1064 nm one produced a similar graph as seen in Figure 18. From Figure 17 and Figure 18 it can be noticed that by taking the average of 100 spectra for each datapoint, the error, i.e. the standard deviation here, becomes very small. The small errorbars underline the importance of averaging multiple LIBS spectra when getting rid of the effects of a difficult sample matrix.

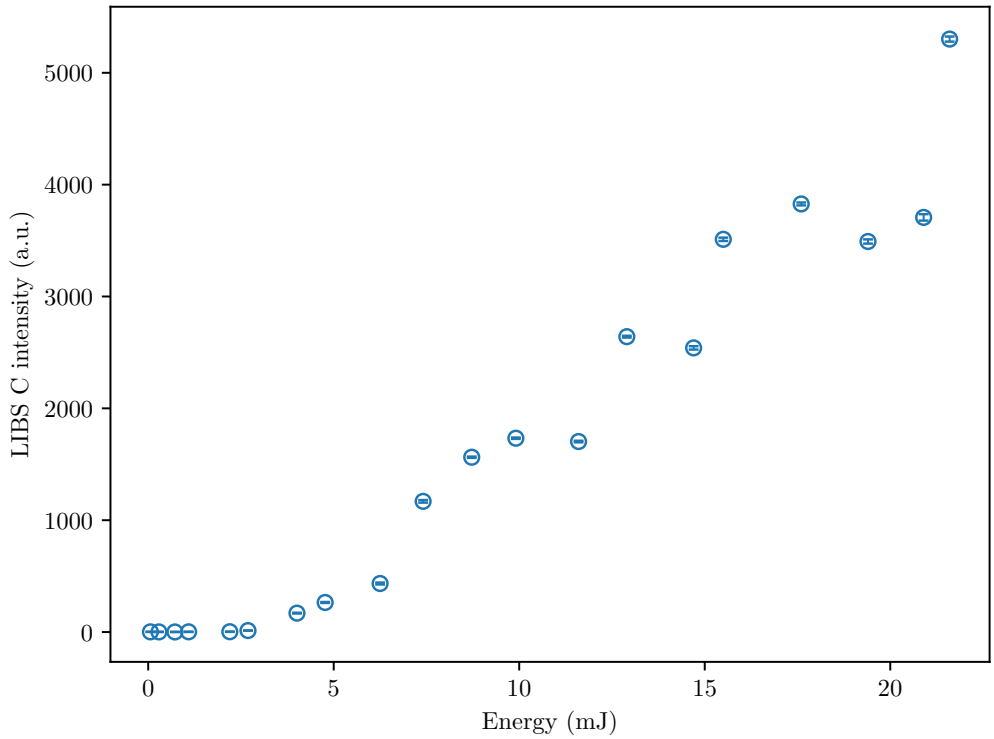

Figure 19. Carbon line intensity as a function of 355 nm laser beam energy of one laser pulse. The energies correspond to energies measured before the final collimating lens, i.e. the energies available for the plasma formation. The line intensities show no sign of saturation which implies that it is safe to use the laser with as high energy as are available. The errorbars here show the standard deviation from the 100 intensities measured for each data point.

7.3 Optimal beam energy

The beam energies introduced here are measured right before the collimating lens. This way the actual energy available for plasma generation is measured. This includes some attenuation from the optical components, most significantly the polarising crystal. The software controlling the attenuation of laser energy was build so that it was possible to set a percentage of the maximum energy wanted from the laser. The energy was varied so that the initial energy was set to be 5 % in the attenuator and it was increased in 5 % steps. Usually spectral signals reach a point of saturation when energy is increased continuously. This can be seen as stabilisation of the signal intensities. The optimal energy to be found here was the energy where the signal intensity reaches its maximal value before it saturates to that value. As can be seen from the Figure 19, the saturation energies were not achieved with the laser using 355 nm beam. This means that the optimal energy for the carbon signal will be the maximal energy of the laser head.

A similar trend was also found by switching the laser wavelength to 1064 nm as seen from Figure 20. Since no saturation was seen in the signal, it was safe to use 100 % of the energy available from the laser head. It must be noted that even though the higher energies seem to give better signal in terms of intensity of the carbon line, it might not be true across the full spectrum. Some other elements might reach saturation much earlier and in finding the optimal laser energy, all the elements of interest must be taken into account. Also even if the intensities get higher as the energy is increased, also broadening mechanisms start to affect the signal. In the case of the carbon line of

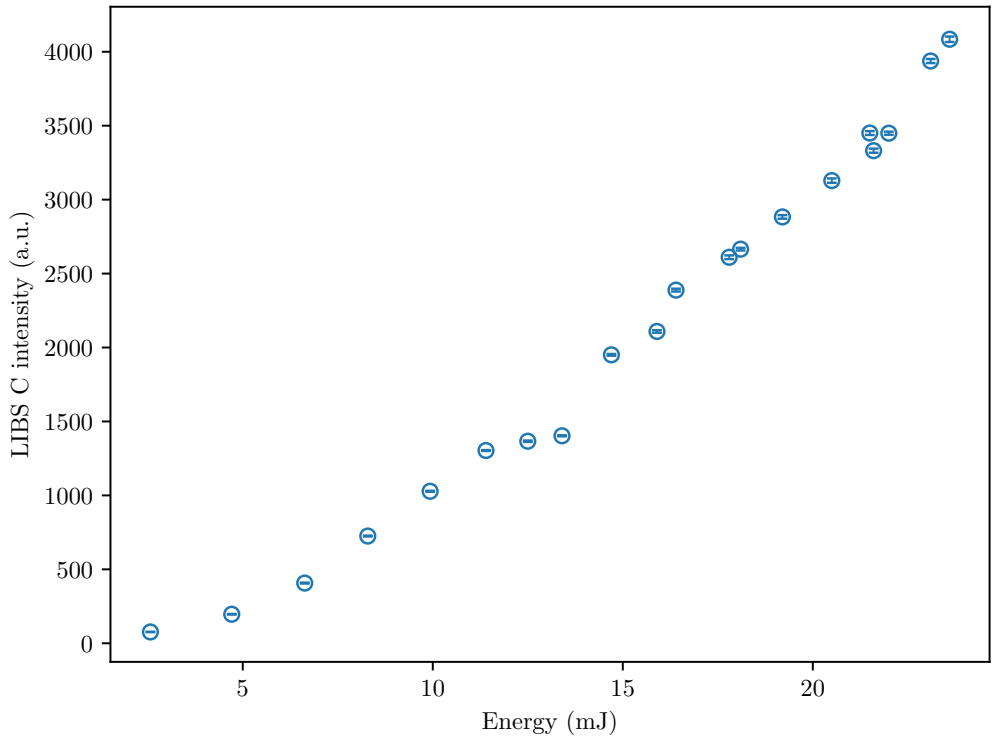

Figure 20. Carbon line intensity as a function of 1064 nm laser beam energy of one laser pulse. The energies correspond to energies measured before the final collimating lens, i.e. the energies available for the plasma formation. The line intensities show no sign of saturation which implies that it is safe to use the laser with as high energy as are available. The errorbars here show the standard deviation from the 100 intensities measured for each data point.

193 nm, no substantial broadening was observed. Similar to the delay measurements, also minimal standard deviations were achieved in the energy measurements by averaging over 100 spectra.

7.4 Calibration curves

Using the values of 200 ns delay, 3.4 µs exposure time and 23.6 mJ pulse energy obtained from the previous measurements, the calibration curves for two separate soil sample sets were created. Both of these sample sets (Qvidja and ML) were reference measured using pyrolysis. The calibration curves were formed by measuring the carbon signal intensity at different pieces of soil collected from the same spot on the field, varying in depth. The reason this was possible was that the concentration varied in the depth profile just enough for a meaningful calibration. The samples were from the surface soil all the way down to 90 cm in depth.

As described in section 3, the goal is to achieve linear, or otherwise predictable, relationship between the measured carbon intensity and the carbon concentration in the soil. The signal along these measurements was varying, mainly due to two reasons: first of all the sample contains inhomogeneities and that is seen in signal as decreasing and increasing line intensity when different parts of soil are being ablated. Another reason is that when shooting the laser pulse many times to the same spot, the plasma is starting to form a little bit above the sample surface due to a crater that the laser pulses eventually form to the sample. Because of the signal variation, no clear relation was found between LIBS signal and the reference concentrations using only the signal of

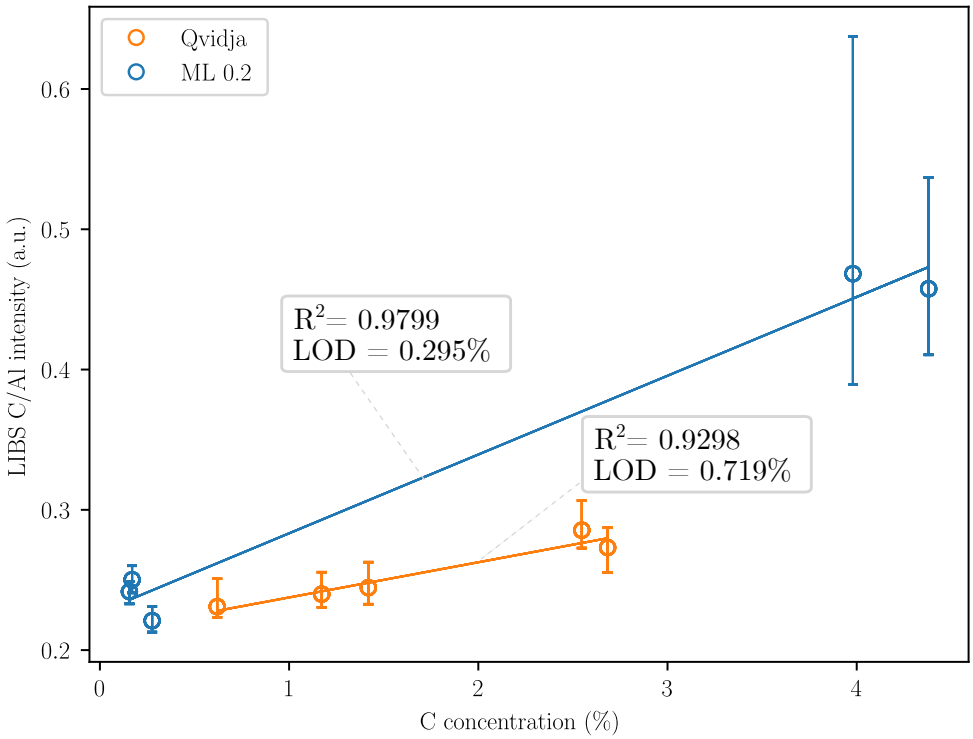

Figure 21. Carbon line intensity normalised by aluminium line intensity as a function of the carbon concentration. Laser was set to 355 nm at the time of measurement. Each point of measured concentration was from the same spot of a field at varying depth. The largest amount of carbon in these samples, especially those of the ML 0.2 field, was at the soil closest to the surface. Surface soil also contains more inhomogeneities compared to the soils from deeper underground and especially the soil from the ML 0.2 field was a lot finer in structure explaining the significant errors in the signal. The error bars here indicate the variation in ten consecutive measurements. The lower limit indicates the lowest value obtained from these ten measurements and similarly the higher limit indicates the highest value obtained from these ten measurements.

carbon, and therefore the internal reference method was tested. Aluminium and silicon were the candidates for the reference elements due to their natural abundance in soil. These were selected also because they have clear spectral lines nearby the carbon line at 193.1 nm. More stable (staying similar in value) the signal of the internal reference is in different depths, the better the linear relation should be. To find the linearised signal, instead of plotting carbon intensity against the carbon concentration, the relative intensity of C/Al was plotted where for the aluminium intensity, the ionic aluminium line at 199.1 nm was used.

Aluminium proved to be effective in linearising the signal as can be seen from the Figures 21 and 22. In the calibration curve measurements, the error bars indicate the error between repetitive measurements. The measurements were repeated ten times and the lower limit of the error bar indicates the lowest value reached in these ten measurements, and similarly the highest value indicates the highest value reached in these ten measurements. There is a large error in the parts of soil richest in carbon, which are found from two samples closest to the surface in the ML sample set. This soil includes a lot of inhomogeneities from various sources. This soil is

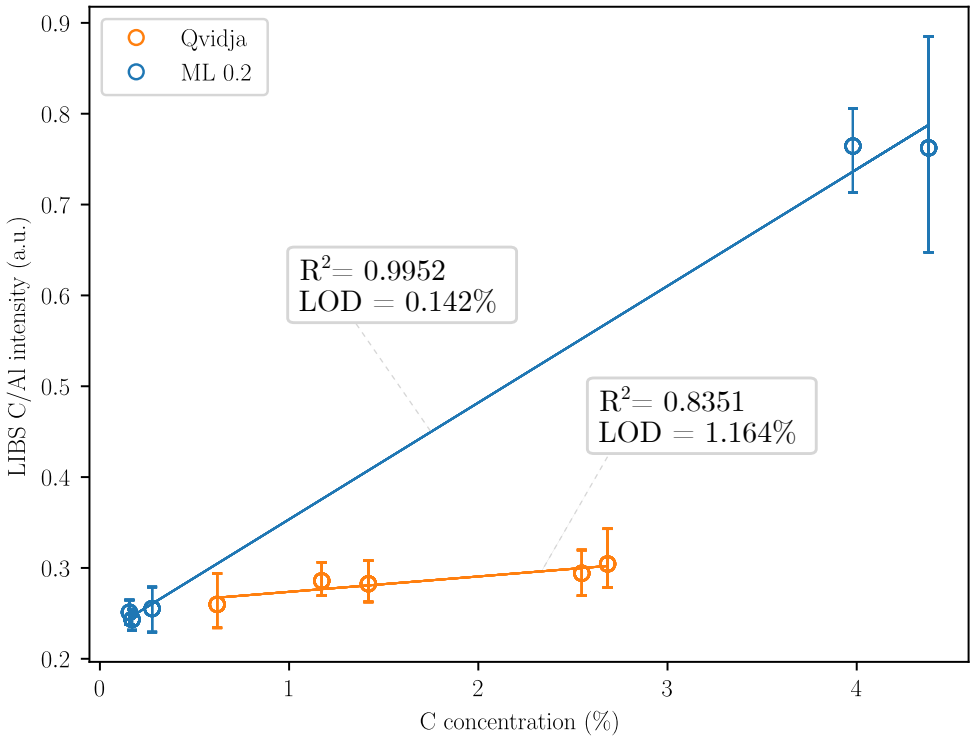

Figure 22. Carbon line intensity normalised by aluminium line intensity as a function of the carbon concentration. Laser was set to 1064 nm at the time of measurement. Each point of measured concentration was from the same spot of a field at varying depth. The largest amount of carbon in these samples, especially those of the ML 0.2 field, was at the soil closest to the surface. Surface soil also contains more inhomogeneities compared to the soils from deeper underground and especially the soil from the ML 0.2 field was a lot finer in structure explaining the significant errors in the signal. The error bars here indicate the variation in ten consecutive measurements. The lower limit indicates the lowest value obtained from these ten measurements and similarly the higher limit indicates the highest value obtained from these ten measurements.

also much more powder-like in structure compared to the more smooth clay-like soils found from deeper. Fine powder-like soil has a tendency to burst a lot more when the laser ligth is focused on it, creating larger craters in the sample compared to a more dense type of soil. For these reasons the the elemental signals fluctuate significantly causing large possible errors in the data. Also it is worth emphasizing, that the downside in linearising the calibration curve is that you have to then measure the intensity or concentration of the internal reference to be able to predict the absolute concentrations of the main element.

Table 5. The figures of merit of the calibration measurements.

	355 nm laser source	1064 nm laser source
ML R^2	0.9799	0.9952
Qvidja R^2	0.9298	0.8351
ML LOD	0.295%	0.142%
Qvidja LOD	0.719%	1.164%

7.5 Wavelength dependency

Comparing the results obtained using different wavelengths, it can be noticed that they follow fundamentally the same trends. Especially regarding the timing and energy measurements this means that not much extra value is gained by manipulating the wavelength of the 1064 nm laser head. This is helpful, since manipulating the wavelength has effect e.g. on the beam profile purity and beam energy. In soil LIBS, the wavelength does not seem to play as important role as the energy density achieved by proper focus of the laser radiation. The ablation efficiency is more dependent on other laser properties such as beam energy. Ablation threshold seems to be slightly higher with the 355 nm laser meaning that more energy is needed to start the ablation. This is visible when comparing the first few datapoints from 355 nm measurement in Figure 17 and the same datapoints in 1064 nm measurement in Figure 18.

Figures of merit of the different calibrations show some differences. The linear regression to the calibration data was done utilizing the linregress[9] function from the Python library SciPy. The limit of detection (LOD) was evaluated using the IUPAC definition from [63]

$$\mathrm{LOD} = \frac{3.3\,\sigma\sqrt{1+\xi}}{b}, \tag{59}$$

where σ stands for the standard deviation of the calibration curve, b is the slope of the calibration curve and ξ is defined by

$$\xi := \frac{\overline{C}}{\sum_i (C_i - \overline{C})^2} \tag{60}$$

where $\overline{C}$ is the average of the concentrations, C_i is the concentration of the ith sample. The coefficients of determination R^2 and LOD for both measurement sets, with 1064 nm laser and 355 nm laser, and both sample sets, Qvidja and ML, are collected in the Table 5. Samples from the ML set have in general smaller errorbars in the 1064 nm laser measurement compared to the 355 nm laser measurement, and it can be most notably seen from the two samples with highest carbon concentration. Also the R^2 value from the 1064 nm laser measurement of ML samples is a bit better with 0.9952 compared to 0.9799 from the 355 nm laser measurement. At the same time the Qvidja samples have a bit worse R^2 value of 0.8351 with the 1064 nm laser source compared to the one from the 355 nm laser measurement of 0.9298. Having smaller errorbars with the ML samples might be an indicator that better ablation is obtained with the 1064 nm laser. Better ablation means that the ablation is more stable in terms of shot-to-shot variation of the laser. When the plasma is similar from pulse to pulse, the repeatability of the measurement gets better and hence the errorbars get smaller, as seen from comparing the Figures 21 and 22.

From Table 5 it can be noticed that in addition to R^2 of the ML calibration being improved with the 1064 nm laser measurement, also the LOD is being improved. At the same time it also gets worse with the Qvidja samples, as did the R^2 value of the Qvidja calibration curve. The reason why the LOD gets worse with the 1064 nm laser is because the slope becomes less steep compared to the 355 nm laser measurement. Steeper curve means that the intercept of the calibration curve becomes higher, which on the other hand means larger LIBS intensity, and hence, error when the concentration of carbon in the sample is zero. An easy fix for this problem would be to have larger set of samples which would include samples with soil carbon percentage closer to zero. More

[9] https://docs.scipy.org/doc/scipy/reference/generated/scipy.stats.linregress.html

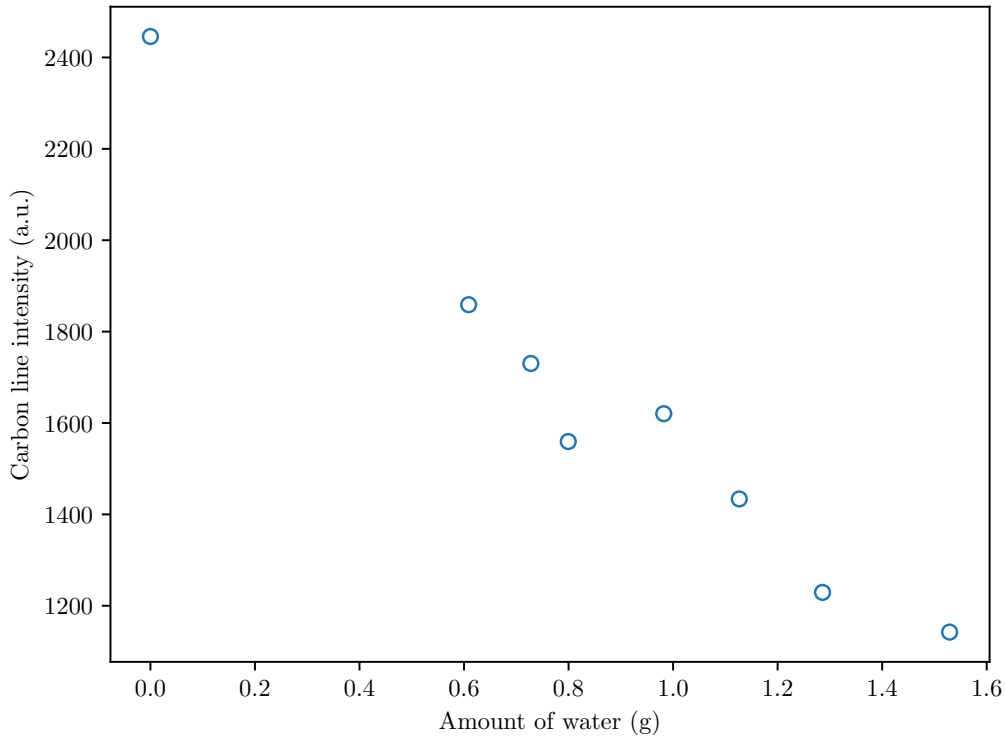

Figure 23. Carbon line intensity with respect to the amount of water in the sample. In this measurement a moist sample was inserted into the setup and a hot air blower dried the sample simultaneously as the spectra were being captured. Increase in the amount of water means that the spectral response decreases.

datapoints would also affect the evaluation of R^2 of the linear fit, possibly also making the difference between the 1064 nm and 355 nm laser measurements smaller in the Qvidja sample set. The variation in repeated measurements of the Qvidja samples does not notably increase or decrease.

7.6 Effects of soil moisture on the signal

Inherent moisture in Finnish soils makes the comparison between the measurements of its constituents problematic. Water in the soils also has deteriorating effects on the ablation efficiency. When the focus of the laser beam is right below the sample surface, the water inside the sample evaporates due to the rising heat of the forming plasma plume. This evaporation creates large craters in the sample which makes the averaging of the data difficult. Also when more energy is used to the phase change of water from liquid to gas, less energy is available for the plasma formation.

When measuring carbon peak at 193.03 nm, it is noticed that it almost disappeared completely when there was water present in the sample. At the same time hydrogen line at 656 nm was becoming more clear. By following the hydrogen line alone, it could be determined whether moisture was deteriorating the spectral signal or not. Figure 23 shows that even fairly small amounts of water already reduced the signal significantly. In the measurement, a hot air blower was drying the moist sample simultaneously as the plasma radiation was being collected. From Figure 24 a) it can be seen that exceptionally wide line of hydrogen appears when the sample is wet and it disappears as the sample dries, as seen from Figure 24 b).

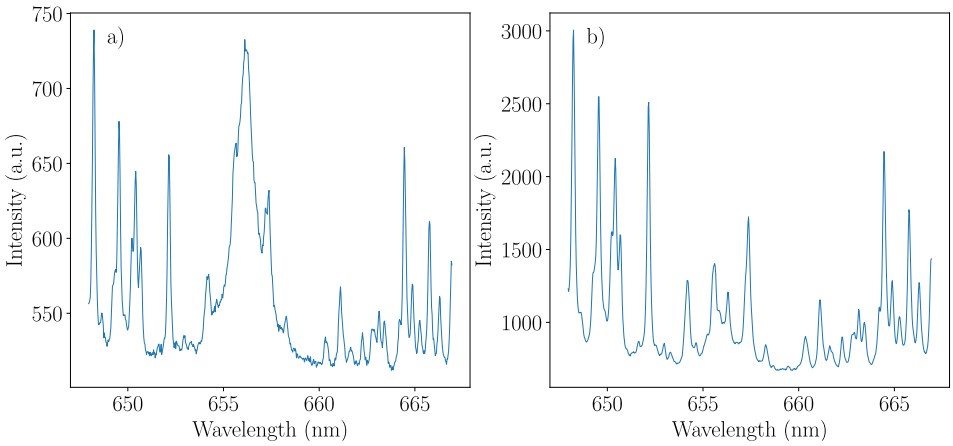

Figure 24. Two figures presenting the hydrogen line intensity at 656 nm with respect to wavelength. The figure a) is captured from a wet soil sample and the hydrogen line of 656 nm is clearly visible. When the same sample was measured dry, the spectrum of figure b) was obtained, and the hydrogen line had disappeared.

The exceptional width of the hydrogen line at around 656 nm compared to the surrounding elemental lines is expected to be the result of the linear Stark effect (57). If it is assumed that other elements around it are affected by other broadening mechanisms, it is likely that the Stark effect is the dominant source of broadening in the hydrogen line. The hydrogen line was still resolved from other lines when the signal got weaker. Due to this, and the difficulty of fitting a function to such a wide peak with other elements mixed in it, the peak value of the hydrogen line was used as the intensity.

7.7 Plasma temperature and electron density

Since the spectral data is now available from multiple different kinds of measurements, it is interesting to see how the plasma, i.e. the plasma temperature and the electron density, evolves when the parameters vary. Here the temperatures and electron densities were evaluated using the Boltzmann plot method (52) and electron density from the Saha distribution (56). Three atomic lines of silicon from Table 4 are used for the temperature evaluation and the atomic line at 212.4 with the ionic line of silicon at 207.2 are used for the electron density evaluation. To test these methods, the data from the measurement where energy was varied was used. Due to the amount of noise at early energies, the methods were tested only on the last 11 data points.

As can be seen from Figure 25, when energy increases from around 16 mJ to 23 mJ, the plasma temperature increases from around 7000 to 8400. The electron densities show an increase from around 10^{13} to 10^{14} cm^{-3}. These values agree in the order of magnitude with the ones given in [46], where plasma temperature in soil measurements is reported around 7000 K and electron density around 0.069×10^{18} cm^{-3}.

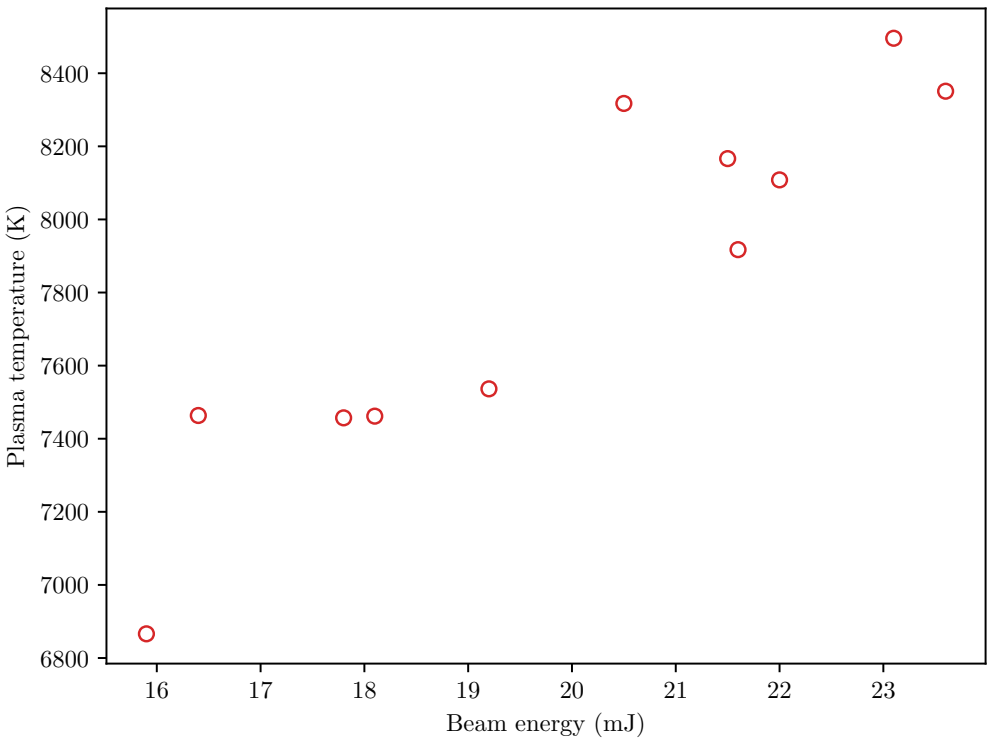

Figure 25. Plasma temperature as a function of laser beam energy. Higher pulse energies produce higher plasma temperatures.

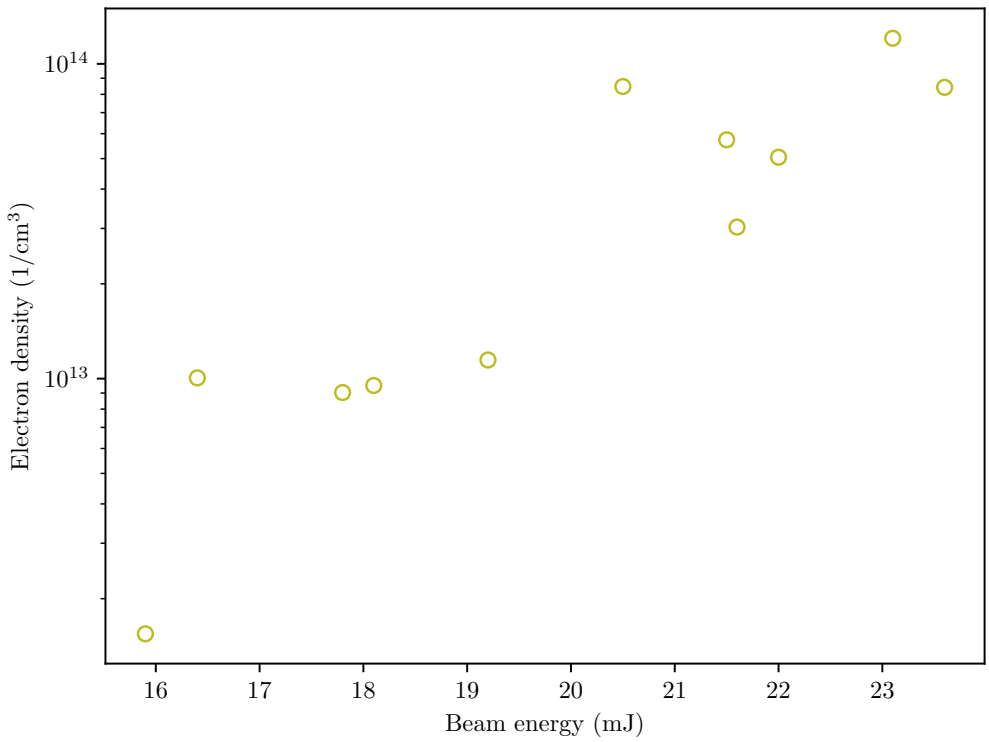

Figure 26. Electron density in the plasma as a function of beam energy. As with the temperature, higher energies result in higher electron densities.

8 Conclusions

The results show that laser-induced breakdown spectroscopy can be utilized for soil carbon assessment and the optimal parameters for that kind of measurement can be found. LIBS sets some requirements on the samples. It was found that if the sample is very powder-like in nature, the shot-to-shot variation of the signal becomes large, resulting in large errors in calibration. That means that samples need to be standardized so that when measured with LIBS, the sample surface should be as smooth as possible and multiple shots should not be shot at the same spot. The repetition rate of 20 Hz was large in the sense that the sample did not have enough time to move to have each of the shots on a fresh surface. This caused variation across all the measurements.

The wavelength was found to have very little effect on the LIBS signal. This is because LIBS as a measurement method is more dependent on the efficiency of the ablation process and plasma formation, and the wavelength does not play so big of a role in it, if the pulse energies of the laser are high enough. The tuning range of energy of the laser used throughout this thesis was enough or even more than enough for the soil carbon assessment. Smaller energies could result in more controlled ablation in the case of powder-like samples. However, in the optimal situation, the beam energy does not need to be varied between samples since this would overly complicate the measurement scenario itself.

The resolution and range of a USB spectrometer shows to be enough for soil carbon LIBS measurements. The resolution of 0.3 nm is enough for the carbon line at 193 nm to resolve from the neighbouring ionized line of aluminium. Also the spectral range covers many of the interesting elemental lines in soils that can be used for other types of analyses from the same measurements. These include for example fertilization residue monitoring or monitoring of toxic elements in soils for soil purity. The Andor spectrograph and ICCD camera used in this thesis were mainly to see whether the behavior of hydrogen at 656 nm is as expected based on the literature and whether this line could be used to compensate the deteriorating effect caused by soil moisture. The most effective way to get rid of the effects of soil moisture was later found to be drying the samples. A heat gun reaching as high as 500°C was able to dry the sample in 20 - 30 seconds. Further research is needed to see if this substantially affects the elemental composition of the sample and whether it can therefore be used in the final application.

When this measurement method is stabilized properly so that the variation of the signal is better controlled, the sample handling is more systematic and the effects of soil moisture can be elegantly removed, LIBS provides a reasonable option for current laboratory standards. As discussed in section 2 the need for a mobile, i.e. field portable, device that can reach the precision competing with the current standards, is clear. When properly developed further, LIBS can be harnessed for field measurements. This is of course not new when considering many other measurements. LIBS appears in handheld devices for metal or mineral analysis and even in rovers, LIBS is used to do elemental detection on Mars. The large scale research on utilizing it for soil measurements, with soil monitoring as the target, has not yet been done.

All of the measurements of this thesis were completed before the May of 2022. Using the setup parameters found in this work: the laser wavelength, laser energy and optimal delay region, another setup was built after this thesis was finished. This setup was designed initially to be more portable for in-situ measurements of soil carbon. A more compact and also more powerful laserhead radiating at 1064 nm is now used for the ablation of the material. Two USB spectrometers similar to the Ibsen one used in this thesis are used to be able to record the full spectrum from 190 nm all the way to 800 nm region. More work has been put into the sample handling also: now the samples are prepared and homogenized in controlled manner, resulting in more stable and comparable measurements. Also a new xy-stage to move the sample has been obtained. The repetition rate of the new laser head is set at 5 Hz, which means that the xy stage can move the sample so that each

pulse hits fresh point on the surface of the sample. This also increases stability in the signal.

The new setup was successfully calibrated without using the method of internal reference [64]. This is mostly due to the increase in the signal stability. The calibration curves follow logarithmic scale with reasonable accuracy, which makes the assessment of soil on a calibrated field possible. Also testing has been done to find whether more global calibration can be found based on, e.g. the soil type. A calibration curve made based on reference measured field was tested on another field that was from totally different place in Finland, but shared the same soil type with the test field. Based on this test, more global calibration based on soil type could be possible, further adding to the merits of LIBS as a measurement method.

LIBS is becoming more and more interesting option in the field of agricultural carbon measurements. It has already successfully solved many of the stumbling blocks of the more traditional methods such as the ones listed in section 3. Compared to the pyrolysis devices such as LECO, LIBS is simple and relatively fast, measurement time being less than one minute per sample. Also calibration from a small sample set from a field is enough and the extensive databases as required by NIR methods are not needed. In addition, the calibration might even hold more generally as the initial results indicate in [64]. Unlike many other methods, LIBS device can also be brought directly to the field to do the measurements on site. In the future the sample handling required by LIBS can be substantially reduced, making LIBS a prominent candidate to be part of the future soil carbon monitoring network.

References

[1] G. S. Senesi and N. Senesi. "Laser-induced breakdown spectroscopy (LIBS) to measure quantitatively soil carbon with emphasis on soil organic carbon. A review". In: *Analytica Chimica Acta* 938 (2016). Cited by: 77, pp. 7–17. DOI: 10.1016/j.aca.2016.07.039.

[2] P. Smith et al. "How to measure, report and verify soil carbon change to realize the potential of soil carbon sequestration for atmospheric greenhouse gas removal". In: *Global Change Biology* 26.1 (2020). Cited by: 203; All Open Access, Green Open Access, Hybrid Gold Open Access, pp. 219–241. DOI: 10.1111/gcb.14815.

[3] G. W. McCarty et al. "Mid-Infrared and Near-Infrared Diffuse Reflectance Spectroscopy for Soil Carbon Measurement". In: *Soil Science Society of America Journal* 66.2 (2002), pp. 640–646. DOI: https://doi.org/10.2136/sssaj2002.6400a. eprint: https://acsess.onlinelibrary.wiley.com/doi/pdf/10.2136/sssaj2002.6400a.

[4] IPCC. *Climate Change 2021: The Physical Science Basis. Contribution of Working Group I to the Sixth Assessment Report of the Intergovernmental Panel on Climate Change*. Ed. by V. Masson-Delmotte et al. New York, Cambridge: Cambridge University Press, 2021. DOI: 10.1017/9781009157896.

[5] IPCC. *Climate Change 2022: Mitigation of Climate Change. Contribution of Working Group III to the Sixth Assessment Report of the Intergovernmental Panel on Climate Change*. Ed. by P. Shukla et al. New York, Cambridge: Cambridge University Press, 2022. DOI: 10.1017/9781009157926.

[6] R. Lal. "Soil carbon sequestration to mitigate climate change". In: *Geoderma* 123.1-2 (2004). Cited by: 2267, pp. 1–22. DOI: 10.1016/j.geoderma.2004.01.032.

[7] IPCC. *IPCC Special Report on Carbon Dioxide Capture and Storage. Prepared by Working Group III of the Intergovernmental Panel on Climate Change*. Ed. by B. Metz et al. New York: Cambridge University Press, 2005.

[8] R. Lal. "Beyond COP21: Potential and challenges of the "4 per Thousand" initiative". In: *Journal of Soil and Water Conservation* 71.1 (2016). Cited by: 164, 20A–25A. DOI: 10.2489/jswc.71.1.20A.

[9] R. Lal. "Soil carbon sequestration impacts on global climate change and food security". In: *Science* 304.5677 (2004). Cited by: 4877, pp. 1623–1627. DOI: 10.1126/science.1097396.

[10] C. Huntingford et al. "Implications of improved representations of plant respiration in a changing climate". In: *Nature Communications* 8.1 (2017). Cited by: 76; All Open Access, Gold Open Access, Green Open Access. DOI: 10.1038/s41467-017-01774-z.

[11] B. Minasny et al. "Soil carbon 4 per mille". In: *Geoderma* 292 (2017). Cited by: 961; All Open Access, Green Open Access, Hybrid Gold Open Access, pp. 59–86. DOI: 10.1016/j.geoderma.2017.01.002.

[12] U. Stockmann et al. "Global soil organic carbon assessment". In: *Global Food Security* 6 (2015), pp. 9–16. ISSN: 2211-9124. DOI: https://doi.org/10.1016/j.gfs.2015.07.001.

[13] C. Bronick and R. Lal. "Soil structure and management: A review". In: *Geoderma* 124.1-2 (2005). Cited by: 2831, pp. 3–22. DOI: 10.1016/j.geoderma.2004.03.005.

[14] A. Ito. "Simulated impacts of climate and land-cover change on soil erosion and implication for the carbon cycle, 1901 to 2100". In: *Geophysical Research Letters* 34.9 (2007). Cited by: 73; All Open Access, Bronze Open Access. DOI: 10.1029/2007GL029342.

[15] N. Batjes. "Total carbon and nitrogen in the soils of the world". In: *European Journal of Soil Science* 47.2 (1996). Cited by: 2388, pp. 151–163. DOI: 10.1111/j.1365-2389.1996.tb01386.x.

[16] J. Dumanski. "Carbon sequestration, soil conservation, and the Kyoto protocol: Summary of implications". In: *Climatic Change* 65.3 (2004). Cited by: 42, pp. 255–261. DOI: 10.1023/B:CLIM.0000038210.66057.61.

[17] K. Paustian et al. "Climate-smart soils". In: *Nature* 532.7597 (2016). Cited by: 1052; All Open Access, Green Open Access, pp. 49–57. DOI: 10.1038/nature17174.

[18] P. Smith et al. "Greenhouse gas mitigation in agriculture". In: *Philosophical Transactions of the Royal Society B: Biological Sciences* 363.1492 (2008). Cited by: 1656; All Open Access, Green Open Access, pp. 789–813. DOI: 10.1098/rstb.2007.2184.

[19] R. J. Zomer et al. "Global Sequestration Potential of Increased Organic Carbon in Cropland Soils". In: *Scientific Reports* 7.1 (2017). Cited by: 224; All Open Access, Gold Open Access, Green Open Access. DOI: 10.1038/s41598-017-15794-8.

[20] D. D. Baldocchi. "Assessing the eddy covariance technique for evaluating carbon dioxide exchange rates of ecosystems: Past, present and future". In: *Global Change Biology* 9.4 (2003). Cited by: 1758, pp. 479–492. DOI: 10.1046/j.1365-2486.2003.00629.x.

[21] J. Hodgkinson and R. P. Tatam. "Optical gas sensing: a review". In: *Measurement Science and Technology* 24.1 (Nov. 2012), p. 012004. DOI: 10.1088/0957-0233/24/1/012004.

[22] J. M. Hollas. *Modern Spectroscopy*. 2010.

[23] V. Bellon-Maurel and A. McBratney. "Near-infrared (NIR) and mid-infrared (MIR) spectroscopic techniques for assessing the amount of carbon stock in soils - Critical review and research perspectives". In: *Soil Biology and Biochemistry* 43.7 (2011). Cited by: 339, pp. 1398–1410. DOI: 10.1016/j.soilbio.2011.02.019.

[24] C. L. Morgan et al. "Simulated in situ characterization of soil organic and inorganic carbon with visible near-infrared diffuse reflectance spectroscopy". In: *Geoderma* 151.3-4 (2009). Cited by: 166, pp. 249–256. DOI: 10.1016/j.geoderma.2009.04.010.

[25] A. Montaser and D. Golightly. *Inductively Coupled Plasmas in Analytical Atomic Spectrometry*. 1987.

[26] J. Mermet. "ATOMIC EMISSION SPECTROMETRY | Inductively Coupled Plasma". In: *Encyclopedia of Analytical Science (Second Edition)*. Ed. by P. Worsfold, A. Townshend, and C. Poole. Second Edition. Oxford: Elsevier, 2005, pp. 210–215. ISBN: 978-0-12-369397-6. DOI: https://doi.org/10.1016/B0-12-369397-7/00032-7.

[27] R. E. Russo et al. "Chapter 3 - Laser ablation". In: *Laser-Induced Breakdown Spectroscopy (Second Edition)*. Ed. by J. P. Singh and S. N. Thakur. Second Edition. Amsterdam: Elsevier, 2007, pp. 41–70. ISBN: 978-0-12-818829-3. DOI: https://doi.org/10.1016/B978-0-12-818829-3.00003-4.

[28] R. S. Harmon, R. E. Russo, and R. R. Hark. "Applications of laser-induced breakdown spectroscopy for geochemical and environmental analysis: A comprehensive review". In: *Spectrochimica Acta Part B: Atomic Spectroscopy* 87 (2013). Thematic Issue: 7th International Conference on Laser Induced Breakdown Spectroscopy (LIBS 2012), Luxor, Egypt, 29 September-4 October 2012, pp. 11–26. ISSN: 0584-8547. DOI: https://doi.org/10.1016/j.sab.2013.05.017.

[29] V. Babushok et al. "Double pulse laser ablation and plasma: Laser induced breakdown spectroscopy signal enhancement". In: *Spectrochimica Acta Part B: Atomic Spectroscopy* 61.9 (2006), pp. 999–1014. ISSN: 0584-8547. DOI: https://doi.org/10.1016/j.sab.2006.09.003.

[30] J. Viljanen, Z. Sun, and Z. T. Alwahabi. "Microwave assisted laser-induced breakdown spectroscopy at ambient conditions". In: *Spectrochimica Acta Part B: Atomic Spectroscopy* 118 (2016), pp. 29–36. ISSN: 0584-8547. DOI: https://doi.org/10.1016/j.sab.2016.02.002.

[31] C. Exley. "Silicon in life : A bioinorganic solution to bioorganic essentiality". In: *Journal of Inorganic Biochemistry* 69.3 (1998), pp. 139–144. ISSN: 0162-0134. DOI: https://doi.org/10.1016/S0162-0134(97)10010-1.

[32] K. Rifai et al. "LIBS core imaging at kHz speed: Paving the way for real-time geochemical applications". In: *Spectrochimica Acta Part B: Atomic Spectroscopy* 150 (2018), pp. 43–48. ISSN: 0584-8547. DOI: https://doi.org/10.1016/j.sab.2018.10.007.

[33] D. Cremers et al. "Measuring total soil carbon with laser-induced breakdown spectroscopy (LIBS)". In: *Journal of Environmental Quality* 30.6 (2001). Cited by: 125, pp. 2202–2206. DOI: 10.2134/jeq2001.2202.

[34] M. Bernoux and C. Cerri. "GEOCHEMISTRY | Soil, Organic Components". In: *Encyclopedia of Analytical Science (Second Edition)*. Ed. by P. Worsfold, A. Townshend, and C. Poole. Second Edition. Oxford: Elsevier, 2005, pp. 203–208. ISBN: 978-0-12-369397-6. DOI: https://doi.org/10.1016/B0-12-369397-7/00245-4.

[35] D. J. Griffiths. *Introduction to Electrodynamics*. 2013.

[36] N. Firouzi Farrashbandi and M. Eslami-Kalantari. "Inverse bremsstrahlung absorption in laser-fusion plasma". In: *Journal of Theoretical and Applied Physics* 14.3 (2020). Cited by: 4, pp. 261–264. DOI: 10.1007/s40094-020-00375-4.

[37] J. Singh and S. Thakur. *Laser-Induced Breakdown Spectroscopy*. Cited by: 860. 2007. DOI: 10.1016/B978-0-444-51734-0.X5001-7.

[38] G. Cristoforetti et al. "Local Thermodynamic Equilibrium in Laser-Induced Breakdown Spectroscopy: Beyond the McWhirter criterion". In: *Spectrochimica Acta - Part B Atomic Spectroscopy* 65.1 (2010). Cited by: 411, pp. 86–95. DOI: 10.1016/j.sab.2009.11.005.

[39] R. Noll. *Laser-induced breakdown spectroscopy: Fundamentals and applications*. Cited by: 579; All Open Access, Green Open Access. 2012, pp. 1–543. DOI: 10.1007/978-3-642-20668-9.

[40] D. W. Hahn and N. Omenetto. "Laser-induced breakdown spectroscopy (LIBS), part I: Review of basic diagnostics and plasmaparticle interactions: Still-challenging issues within the analytical plasma community". In: *Applied Spectroscopy* 64.12 (2010). Cited by: 816, 335A–366A. DOI: 10.1366/000370210793561691.

[41] J. van der Mullen. "On the atomic state distribution function in inductively coupled plasmasI. Thermodynamic equilibrium considered on the elementary level". In: *Spectrochimica Acta Part B: Atomic Spectroscopy* 44.11 (1989), pp. 1067–1080. ISSN: 0584-8547. DOI: https://doi.org/10.1016/0584-8547(89)80107-7.

[42] R. McWhirter. "Chapter 5". In: *Plasma Diagnostics Techniques*. Ed. by R. Huddleston and S. Leonard. 1965, pp. 201–264.

[43] H. R. Griem. "Validity of Local Thermal Equilibrium in Plasma Spectroscopy". In: *Phys. Rev.* 131 (3 1963), pp. 1170–1176. DOI: 10.1103/PhysRev.131.1170.

[44] W. T. Chan and R. E. Russo. "Study of laser-material interactions using inductively coupled plasma-atomic emission spectrometry". In: *Spectrochimica Acta Part B: Atomic Spectroscopy* 46.11 (1991). Cited by: 99, pp. 1471–1486. DOI: 10.1016/0584-8547(91)80199-D.

[45] R. E. Russo. "Short-pulse LIBS: fundamentals and applications". In: *Laser Induced Breakdown Spectroscopy*. Ed. by A. W. Miziolek, V. Palleschi, and I. Schechter. Cambridge University Press, 2006, pp. 477–489. DOI: 10.1017/CBO9780511541261.014.

[46] D. A. Cremers and L. J. Radziemski. *Handbook of Laser-induced Breakdown Spectroscopy*. Cited by: 1612. 2006, pp. 1–283. DOI: 10.1002/0470093013.

[47] E. Tognoni et al. *From sample to signal in laser-induced breakdown spectroscopy: A complex route to quantitative analysis*. Vol. 9780521852746. Cited by: 70. 2006, pp. 122–170. DOI: 10.1017/CBO9780511541261.004.

[48] A. Ciucci et al. "New Procedure for Quantitative Elemental Analysis by Laser-Induced Plasma Spectroscopy". In: *Applied Spectroscopy* 53.8 (1999), pp. 960–964. DOI: 10.1366/0003702991947612.

[49] T. Völker and I. B. Gornushkin. "Importance of physical units in the Boltzmann plot method". In: *Journal of Analytical Atomic Spectrometry* 37.10 (2022). Cited by: 1; All Open Access, Hybrid Gold Open Access, pp. 1972–1974. DOI: 10.1039/d2ja00241h.

[50] C. Aragón and J. Aguilera. "Characterization of laser induced plasmas by optical emission spectroscopy: A review of experiments and methods". In: *Spectrochimica Acta Part B: Atomic Spectroscopy* 63.9 (2008), pp. 893–916. ISSN: 0584-8547. DOI: https://doi.org/10.1016/j.sab.2008.05.010.

[51] H. R. Griem, A. C. Kolb, and K. Shen. "Stark broadening of hydrogen lines in a plasma". In: *Physical Review* 116.1 (1959). Cited by: 149, pp. 4–16. DOI: 10.1103/PhysRev.116.4.

[52] H. R. Griem. *Spectral Line Broadening by Plasmas*. 1974.

[53] V. T. Aaltonen et al. "Maaperäsanaston ja maalajien luokituksen tarkistus v. 1949". In: *Agricultural and Food Science* 21.1 (Jan. 1949), pp. 37–66. DOI: 10.23986/afsci.71269.

[54] K.-H. Korhonen, R. Gardemeister, and M. Tammirinne. *Geotekninen maaluokitus*. Finnish. Valtion teknillinen tutkimuskeskus: Geotekniikan laboratorio. Tiedonanto 14. Finland: VTT Technical Research Centre of Finland, 1974. ISBN: 951-38-0096-2.

[55] Soil Survey Staff. *Soil taxonomy: A basic system of soil classification for making and interpreting soil surveys. 2nd edition. Natural Resources Conservation Service. U.S. Department of Agriculture Handbook 436.* 1999.

[56] H. Lilja et al. *Suomen maannostietokanta: Käyttöopas versio 1.1*. suomi. Luonnonvara- ja biotalouden tutkimus 6. Suomi: Luonnonvarakeskus (Luke), May 2017. ISBN: 978-952-326-356-7.

[57] J. E. Cano Bernal, K. Rankinen, and S. Thielking. "Concentration of organic carbon in Finnish catchments and variables involved in its variations". In: *Journal of Environmental Management* 302 (2022), p. 113981. ISSN: 0301-4797. DOI: https://doi.org/10.1016/j.jenvman.2021.113981.

[58] C. Reimann et al., eds. *Chemistry of Europe's Agricultural Soils, Part A*. Stuttgart, Germany: Schweizerbart Science Publishers, Apr. 2014. ISBN: 9783510968466.

[59] M. Yli-Halla and D. L. Mokma. "Classification of Soils of Finland According to Soil Taxonomy". In: *Soil Survey Horizons* 40.2 (1999), pp. 59–69. DOI: https://doi.org/10.2136/sh1999.2.0059.

[60] O. Nevalainen et al. "Towards agricultural soil carbon monitoring, reporting, and verification through the Field Observatory Network (FiON)". In: *Geoscientific Instrumentation, Methods and Data Systems* 11.1 (2022), pp. 93–109. DOI: 10.5194/gi-11-93-2022.

[61] V. Bulatov, L. Xu, and I. Schechter. "Spectroscopic Imaging of Laser-Induced Plasma". In: *Analytical Chemistry* 68.17 (1996). Cited by: 61, pp. 2966–2973. DOI: 10.1021/ac960277a.

[62] M. Kneen and H. Annegarn. "Algorithm for fitting XRF, SEM and PIXE X-ray spectra backgrounds". In: *Nuclear Instruments and Methods in Physics Research Section B: Beam Interactions with Materials and Atoms* 109-110 (1996), pp. 209–213. ISSN: 0168-583X. DOI: https://doi.org/10.1016/0168-583X(95)00908-6.

[63] F. Poggialini et al. "Calculating the Limits of Detection in Laser-Induced Breakdown Spectroscopy: Not as Easy as It Might Seem". In: *Applied Sciences (Switzerland)* 13.6 (2023). Cited by: 2; All Open Access, Gold Open Access. DOI: 10.3390/app13063642.

[64] V. Dwivedi et al. "Optical assessment of the spatial variation in total soil carbon using laser-induced breakdown spectroscopy". In: *Geoderma* 436 (2023), p. 116550. ISSN: 0016-7061. DOI: https://doi.org/10.1016/j.geoderma.2023.116550.

[65] D. W. Hahn and N. Omenetto. "Laser-induced breakdown spectroscopy (LIBS), part II: Review of instrumental and methodological approaches to material analysis and applications to different fields". In: *Applied Spectroscopy* 66.4 (2012). Cited by: 1115, pp. 347–419. DOI: 10.1366/11-06574.

[66] IPCC. *Climate Change 2001: The Scientific Basis. Contribution of Working Group I to the Third Assessment Report of the Intergovernmental Panel on Climate Change*. Ed. by J. Houghton et al. New York: Cambridge University Press, 2001. DOI: 10.1017/9781009157926.